UNIVERSITY OF CALIFORNIA SAN DIEGO

The effects of brain state and behavioral relevance on sensory representations in awake mouse auditory cortex

A dissertation submitted in partial satisfaction of the requirements for the degree Doctor of Philosophy

in

Neurosciences

by

Pei-Ann Lin

Committee in charge:

Professor Jeffry S. Isaacson, Chair
Professor Edward M. Callaway
Professor Timothy Q. Gentner
Professor Christina M. Gremel
Professor Roberto Malinow

2019

Copyright

Pei-Ann Lin, 2019

All Rights Reserved

The Dissertation of Pei-Ann Lin is approved, and it is acceptable in quality and form for publication on microfilm and electronically:

_____

_____

_____

_____

_____
Chair

University of California San Diego

2019

DEDICATION

I would like to dedicate this body of work to two kind-hearted and meticulous scientists who have fundamentally shaped the manner in which I think about and communicate data. To Dr. Xu Liu—thank you for believing in me and showing me the epitome of compassion, intellect, and mentorship. The world is a measurably bleaker place without you in it. To Dr. Jeffry Isaacson—thank you for taking a chance on me as a student. Thank you for your patience, guidance, and generosity. It was a true privilege to have been a member of your lab.

I would also like to whole-heartedly thank my wonderful network of family and friends that supported me through the ups and downs of graduate school. To my dad—thank you for instilling in me a strong work ethic and curiosity about the world. You were the first scientist in my life and are an inspiration. To my mom—thank you for instilling in me a strong passion for teaching. To Pei-Hsin—thank you for your generosity and continually pushing me to achieve beyond what I ever thought I could be capable of. To Jen-Lee—you're the best twin brother anyone could ask for. Thanks for always being just a phone call away. To Bryce—thank you for supporting me intellectually, emotionally, and financially through 6 years of life, love, and grad school. Looking forward to starting new adventures together! And finally, to my furry dorks Charlie and Lenny—thanks for the constant kitty therapy…you shall continue to be rewarded with mountains of catnip.

EPIGRAPH

You never won’t know what you can’t achieve until you don’t achieve it.

Chris Parnell as Mr. Gordon, 21 Jump Street (2012)

TABLE OF CONTENTS

LIST OF FIGURES

LIST OF TABLES

ACKNOWLEDGEMENTS

I would like to acknowledge the members of the Isaacson lab for their support over the past few years. In particular, I'd like to thank my advisor, Jeffry Isaacson, for his dedication and patience in teaching and mentorship and my co-author, Sam Asinof, for his intellectual contributions. Furthermore, I'd like to thank the undergraduate researchers and technicians for their assistance with various aspects of various projects: Kimi Taira, Mandy Lai, Marissa Justen, Chris Song, and Elena Westeinde. I would also like to acknowledge generous funding from the National Science Foundation Graduate Research Fellowship program.

VITA

2008-2012	Bachelor of Science, Massachusetts Institute of Technology
2012-2013	Research Technician, Picower Institute
2013-2019	Doctor of Philosophy, University of California San Diego
2019-	Consultant, Boston Consulting Group – Los Angeles

PUBLICATIONS

Brigidi GS, Hayes MGB, Hartzell AL, Texari L, **Lin PA**, Bartlett A, Ecker JR, Benner C, Heinz S, Bloodgood BL. (2019) Genomic decoding of neuronal depolarization by stimulus-specific NPAS4 heterodimers. *bioRxiv*.

Ramirez S*, Liu X*, **Lin PA**, Suh J, Pignatelli M, Redondo RL, Ryan TJ, Tonegawa S. (2013) Creating a false memory in the hippocampus. *Science, 341*(6144), 387-391.

Baratta MV, Kodandaramaiah SB, Yao J, Weber MD, **Lin PA**, Gisabella B, Petrossian N, Amat J, Kim K, Yang A, Forest CR, Boyden ES, Goosens KA. (2015) Stress enables reinforcement-elicited serotonergic consolidation of fear memory. *Biol Psych, 79*(10), 814-822.

ABSTRACT OF THE DISSERTATION

The effects of brain state and behavioral relevance on
sensory representations in awake mouse auditory cortex

by

Pei-Ann Lin

Doctor of Philosophy in Neurosciences

University of California San Diego, 2019

Professor Jeffry S. Isaacson, Chair

Sensory representations in the brain are constantly modulated by a variety of factors such as brain state and behavioral context. This dissertation seeks to build a deeper understanding of how our brains accurately represent the world around us by utilizing two-photon calcium imaging of awake mouse auditory cortex during passive listening and learning. I begin with an overview of the anatomical organization of primary auditory cortex (A1) projection neurons. By using spectrally-distinct retrograde tracers, I labeled projection populations from A1 to three functionally distinct brain regions: caudate putamen, inferior colliculus, and contralateral A1. By visualizing the distribution of and overlap between each tracer, I found that the spatial organization of these projection populations were markedly distinct, and labeled neurons rarely projected to more than one target region. These results suggest that A1 projections are organized in a manner that is conducive to target-relevant information transfer. Next, I functionally characterized projections from the lateral amygdala (LA), a structure implicated in

emotion processing, to secondary auditory cortex (A2). I observed that discriminative auditory fear conditioning (DAFC) bidirectionally modulates the strength of A2 amygdalar axon responses to the aversive (CS+) and neutral (CS-) tones. Additionally DAFC-related plasticity was not sufficient for immediately driving expression of discriminative fear behavior, suggesting that LA serves as a primary site of discriminative fear memory. Follow-up experiments characterizing the effects of DAFC on local A2 neurons are necessary in order to fully appreciate the significance of these preliminary findings. Finally, I investigated whether arousal state modulates A1 sensory representations. Pyramidal cell response strength and reliability increased with arousal, resulting in broader frequency tuning and stronger signal correlations. Although this increase in tuning overlap, in isolation, would be detrimental to frequency discrimination, nonlinear classifier decoding accuracy improves with arousal. To reconcile this discrepancy, I delved deeper into the effects of arousal on population activity and found that noise correlations decrease for cells that show stronger signal correlations and increase for cells that show weaker signal correlations as arousal increases. This divergence in correlations has been shown both theoretically and experimentally to improve stimulus discrimination. Taken together, arousal strengthens A1 layer 2/3 tone-evoked responses and modulates inter-neuronal correlations in a nuanced manner that ultimately improves frequency discrimination.

CHAPTER 1: Anatomical organization and response properties of A1 projection neurons

Abstract

Sensory information processed in the auditory cortex (AC) is directed to a variety of spatially and functionally distinct targets, including contralateral AC, amygdala, inferior colliculus, striatum, and thalamus. These areas play distinct roles in sound-guided behavior and cognition. However, it is unclear whether the organization of AC projections supports transmission of redundant auditory information to all target regions or transmission of specific aspects of auditory information to different target regions. To address this question, we used a retrograde tracer, cholera toxin B (CTB), conjugated to several different fluorescent markers to visualize and characterize the spatial overlap of AC projection subpopulations. We subsequently used two-photon calcium imaging to characterize the response properties of Layer 2/3 projection subpopulations in primary auditory cortex (A1) of awake mice.

Introduction

Sensory processing in the brain requires coordination of information transfer across a variety of functionally distinct structures and cell types. To investigate the spatial and functional organization of AC projection neurons, we began by visualizing projections from A1 to downstream regions. Similar to other parts of the sensory cortices, the AC can be divided into a few major auditory subregions (Figure 1.1A). Intrinsic imaging through the skull of anesthetized mice (Figure 1.1B) allows for reliable identification of these subregions, including primary auditory cortex (A1, secondary auditory cortex (A2), and the anterior auditory field (AAF). We then injected a cell-filling tdT-tomato virus in A1, which allowed for visualization of axons departing A1 and terminating in downstream regions. Regions with significant input from A1 included the ipsilateral medial geniculate nucleus of the thalamus (Figure 1.1C), the ipsilateral inferior colliculus (Figure 1.1D), the caudate putamen, the ventral posterior nucleus of the thalamus (Figure 1.1E), and contralateral A1 (Figure 1.1F).

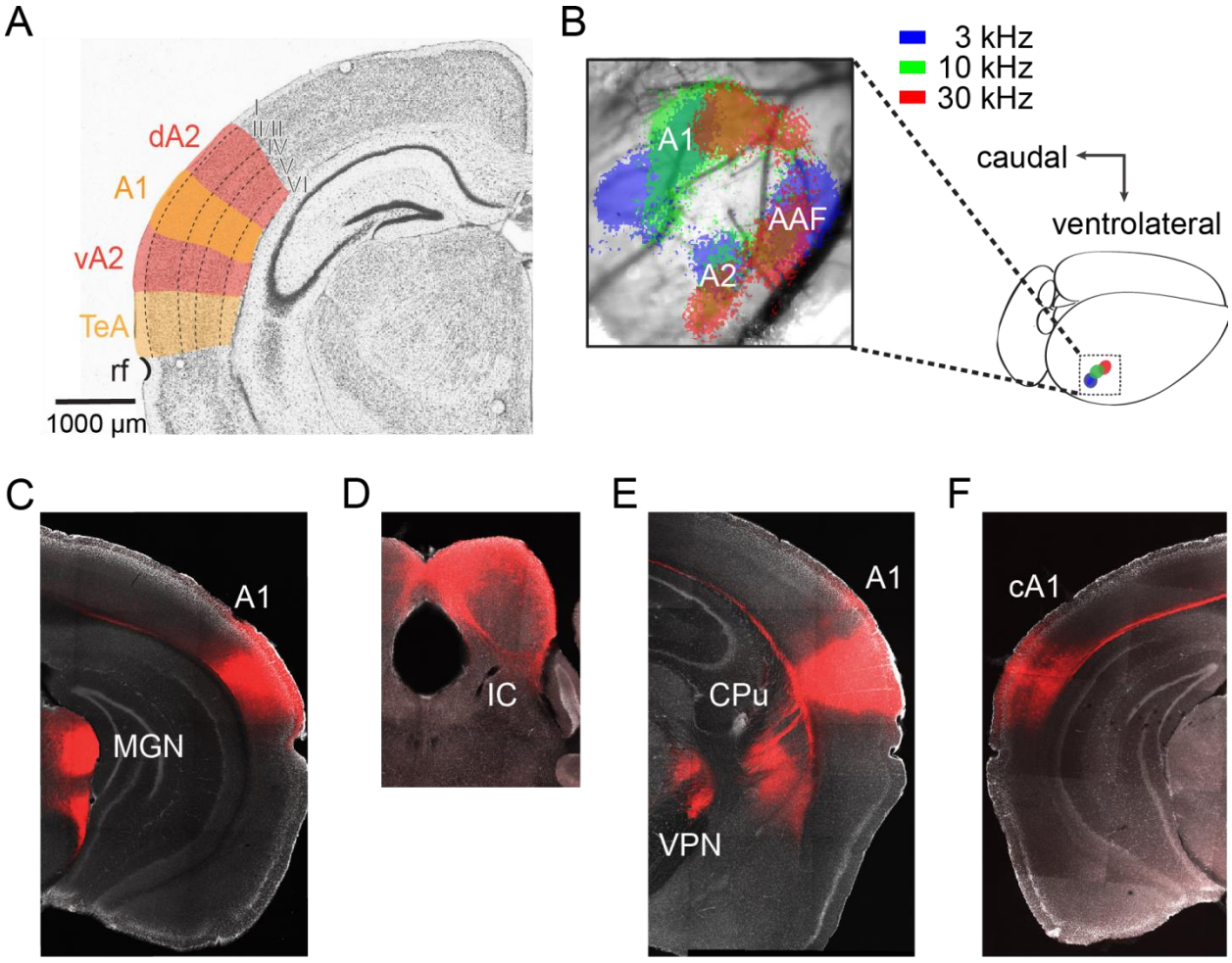

Figure 1.1. A1 projections target many functional distinct downstream brain regions. (A) The major subregions and laminar organization of the auditory cortex (AC). Background image of coronal slice adapted from the Allen Brain Institute Mouse Atlas. (B) Auditory cortex subregions identified by intrinsic imaging. (C) AAV-2.1-CAG-tdTomato injected unilaterally in each of three A1 tonotopic subregions. Tissue was fixed, sectioned and imaged on a confocal microscope. A1 projections were observed in ipsilateral medial geniculate nucleus of the thalamus (MGN), (D) inferior colliculus (IC), (E) caudate putamen of the striatum (CPu), and ventral posterior nucleus of the thalamus (VPN). (F) Projections were also observed in contralateral A1 (cA1). *A1 - primary auditory cortex; dA2 - dorsal secondary auditory cortex; vA2 - ventral secondary auditory cortex; TeA - temporal association cortex; rf - rhinal fissure.*

The projection targets of A1 are known to play a variety of distinct roles. For example, the caudate putamen is implicated in auditory processing (Guo et al., 2018; LeDoux et al., 1991) while projections from A1 to caudate putamen in rats are specifically thought to mediate decision making bias in an auditory discrimination task (Znamenskiy and Zador, 2013). Furthermore, A1 projections to the inferior colliculus have been reported to be both necessary

and sufficient for driving innate flight behavior in response to sudden, high-intensity noise (Xiong et al., 2015). While these studies address sensory responses of auditory cortex projections during active behavior, we hypothesize that tuning to pure tone frequency during passive listening may also differ between A1 projection subtypes. In fact, *in vivo* whole cell voltage clamp recordings in anesthetized rat A1 has revealed that AC layer V regular-spiking (RS) neurons exhibit much sharper frequency tuning and well-matched excitatory and inhibitory intracortical inputs compared to layer V intrinsic bursting (IB) neurons, which display early and unselective responses to a broad range of sound frequencies and have inhibitory inputs that are more narrowly tuned than their excitatory inputs (Sun et al., 2013). Additionally, RS and IB cells are morphologically distinct and are known to project to subcortical nuclei and contralateral cortex, respectively.

While corticotectal, corticostriatal, and corticocortical cells in the visual cortex are known to exhibit differences in spatial organization, contrast thresholds, and tuning broadness for orientation and spatial frequency (Kim et al., 2015; Lur et al., 2016; Wang and Burkhalter, 2013), knowledge about the manner in which A1 pyramidal cells are spatially distributed and the extent to which they encode and deliver distinct features of auditory processing to downstream structures remains incomplete. Thus, in this study, we use a combination of retrograde tracing and two-photon calcium imaging in order to further address these questions.

Results

We first investigated the spatial organization of A1 projection neurons by injecting the retrograde tracers CTB-488, CTB-555, CTB-647 in left A1, right caudate putamen, and right inferior colliculus (Figure 1.7A). After tissue fixation and slicing on a microtome, 100 um coronal slices were imaged using a Keyence epifluorescence microscope. Custom MATLAB GUIs were used for measuring laminar depth and dorsoventral location, and the Allen Brain Institute Mouse Atlas and stereotaxic coordinates were used to estimate the rostrocaudal location of each cell. Strikingly, very few labeled cells appeared to project to more than one of the three selected A1 target regions (Figure 1.7B). Labeled projections appeared predominantly corticostriatal (58.8%), while labeled corticocortical projections (24.5%) outnumbered labeled corticotectal cells (16.6%). A three-dimensional rendering of each right AC cell's location (Figure 1.7C) revealed markedly distinct distributions of each projection population along all three axis. As expected, corticotectal cells were confined to layer V of the AC, and corticocortical cells were limited to putative A1. Corticostriatal cells appeared to span the majority of AC, with higher density ventrally and rostrally. Taken together, these results suggest that the labeled cells are likely to be organized in a manner that is conducive to delivery of target-specific auditory information to downstream regions.

To investigate potential functional differences between projection cell types in A1, we next examined pure tone frequency tuning in A1 layer II/III corticocortical and corticostriatal cells (Figure 1.A). Mice expressing the calcium indicator GCaMP6s in all cortical excitatory cells were injected with CTB-555 in either left A1 or right caudate putamen prior to chronic imaging window implantation (Figure 1.8A-B). During a 1-2 week post-operative recovery period, mice were intrinsic imaged to identify right A1 and habituated to head fixation under a two-photon microscope. During each imaging session, randomly-ordered pure tones of 17 logarithmically-spaced frequencies ranging from 2 kHz to 40 kHz and 3 sound pressure levels (30, 50, 70 dB)

were each presented from an electrostatic speaker positioned contralateral to the imaging field of view (Figure 1.8-A).

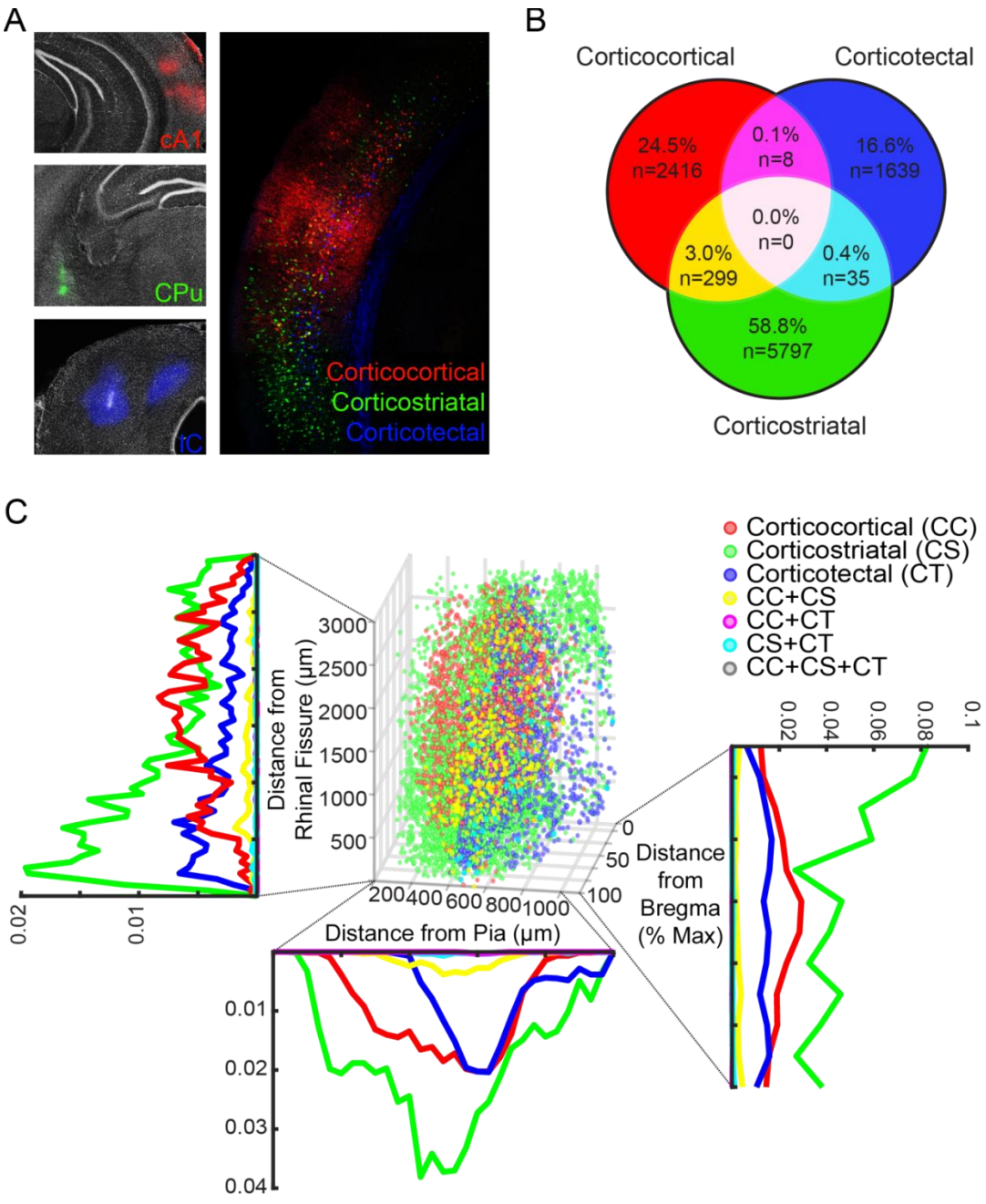

Figure 1.2. A1 projection populations are spatially distinct and primarily target one downstream brain region. (A) Representative images of injection sites (left) and CTB-labeled AC projection subpopulations (right). CTB-488, CTB-555, and CTB-647 were injected in contralateral A1, ipsilateral CPu, and ipsilateral IC, respectively. (B) AC projection neurons rarely target more than one downstream region (n = 9852 cells; 1 mouse). (C) 3D reconstruction and relative frequency distribution of cells along each spatial dimension reveals distinctly distributed AC projection subpopulations.

Imaged cells that appeared labeled with both CTB and GCaMP6s were assumed to be A1 projection neurons with known targets after confirming accurate targeting of CTB-555 injections in fixed tissue (Figure1.8C). To ensure that the presence of CTB was not adversely affecting the health of A1 layer II/III pyramidal cells, we first quantified the percent of tone-responsive cells in each imaging field of view (Figure1.8D). Both unlabeled cells and CTB-labeled cells appeared to yield an approximately similar percentage of tone-response cells; thus, CTB is unlikely to significantly affect the health of neurons within 2-3 weeks of injection.

While visualization of tonal receptive fields (TRFs) for corticostriatal and corticocortical cells revealed cells tuned to a variety of characteristic frequencies (Figure 1.8E-F), the average TRF for both CTB-labeled populations and unlabeled populations appeared to be indistinguishable in shape and frequency tuning broadness. Using an equation for calculating lifetime sparseness, a measure of tuning broadness that is independent of TRF shape, the tuning broadness between corticostriatal, corticocortical, and unlabeled was indeed found to be highly similar (Figure 1.8G). Taken together, passive tuning to pure tone frequency does not differ between A1 excitatory corticostriatal and corticocortical cells despite their unique spatial distributions across the auditory cortex.

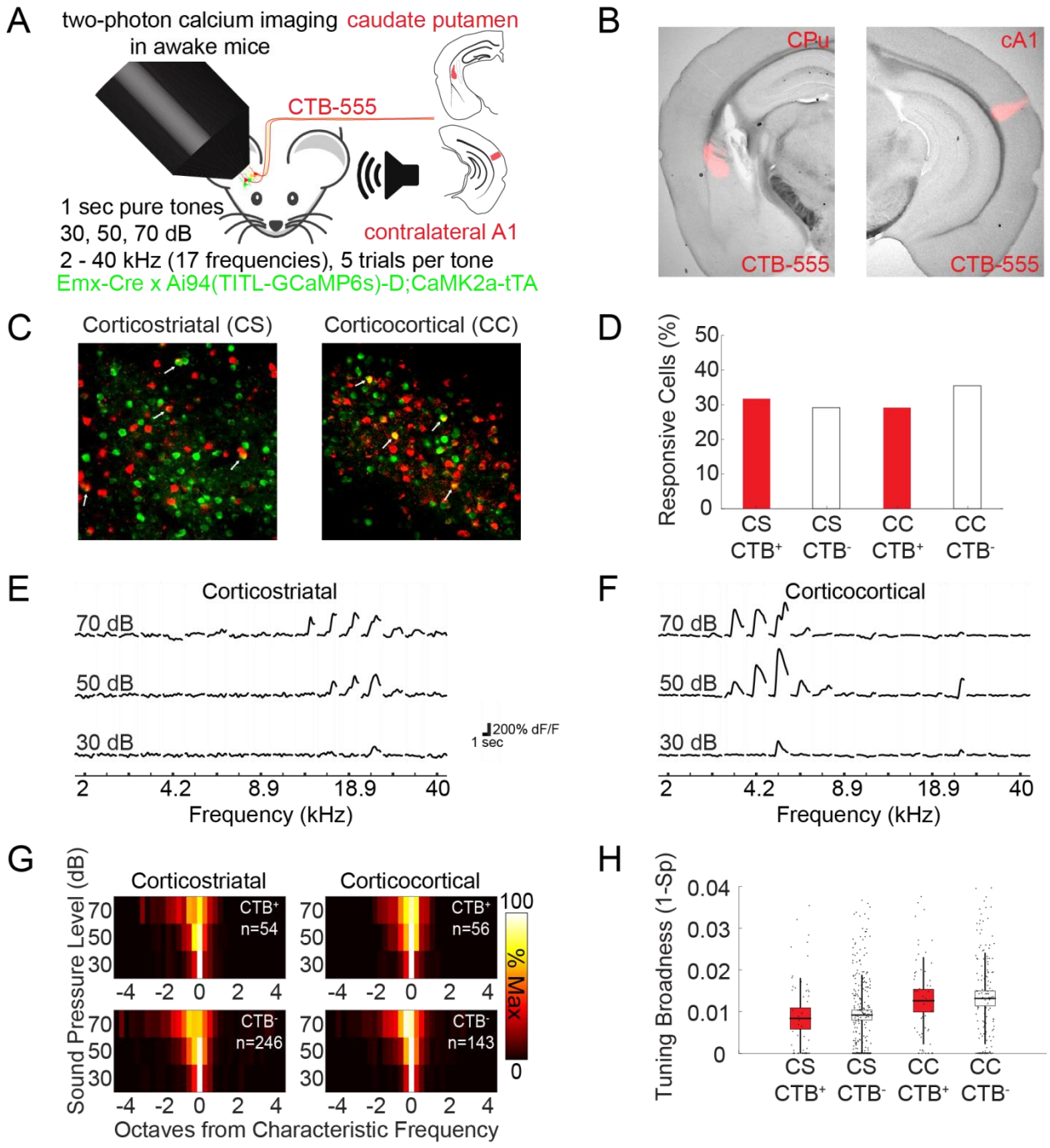

Figure 1.3. Pure tone frequency selectivity is indistinguishable between A1 layer 2/3 corticostriatal and corticocortical projections. (A) Schematic for calcium imaging experiments. (B) Representative images of CTB-555 injection sites from two mice. (C) Representative calcium imaging fields of view. (D) Fraction of tone-responsive cells for CTB-labeled and unlabeled cell populations. (E) Average responses for a representative corticostriatal cell and (F) corticocortical cell. (G) Heatmaps of average tonal receptive fields. (H) Tuning broadness as measure by lifetime sparseness (Sp).

Discussion

Our findings suggest A1 projections rarely target more than one of three labeled downstream regions and are thus organized in a manner that may support transmission of unique subsets of auditory information to functionally distinct areas of the brain. However, our preliminary findings also indicate that frequency selectivity to pure tones is very similar for layer II/III corticostriatal and corticocortical projection neurons. Whether corticotectal cells would exhibit distinct frequency selectivity relative to other target-specific projection populations remains to be addressed, and although not explored in the current study, it is possible that responses to features of other auditory stimuli for corticostriatal and corticocortical cells would differ during passive listening. Additionally, sensory representations during active behavior (e.g. a discriminative auditory task) could be distinct for A1 projection neurons depending on their downstream targets.

Finally, an advanced labeling technique called MAPSeq, which combines barcoding of thousands of projection neurons with unique RNA sequences and *in situ* hybridization of detection of mRNA, was recently developed to address the spatial organization of many projection neuron populations with high accuracy and at a much larger scale (Chen et al., 2018). However, although labeling of projection populations with CTB is known to underrepresent the cells of interest, CTB labeling still holds an advantage over both MAPSeq and retrograde viral labeling due to short expression lead time and minimal toxicity to cells. As such, the retrograde labeling methods in the current study remain a viable approach for the purposes of addressing sensory representations in select populations of projections in awake and behaving mice.

Experimental Procedures

Animals. All procedures were in accordance with protocols approved by the UCSD Institutional Animal Care and Use Committee and guidelines of the National Institute of Health. Mice were acquired from Jackson Laboratories (C57BL/6 (Jax: 000664); Emx1-Cre x CaMKII-tTA x Ai94 (Jax: 024115)) and housed in a room with a reversed light cycle. Experiments were performed during the dark period. Mice of both genders were used for experiment at postnatal ages of 8-16 weeks.

Intrinsic imaging. Intrinsic signal images were acquired using a tandem lens macroscope and 12 bit, CCD camera (CCD-1300QF, VDS Vosskühler). Mice were first isoflurane-anesthetized and surgerized to expose the skull surrounding left auditory cortex. Images of surface vasculature were acquired using green LED illumination (540 nm) and intrinsic signals were recorded (27 Hz) using red illumination (615 nm). Each trial consisted of 1-sec baseline followed by a 1-sec sound stimulus (70 dB pure tone with a frequency of 3, 10, or 30 kHz, 20 trials for each frequency) and 30-sec inter-trial interval. Images of reflectance (R) were acquired at 1024 × 1024 pixels and downsampled to 512 × 512 pixels by bilinear interpolation. Images during the response period (0.5–2 sec from the sound onset) were averaged and divided by the average image during the baseline. Images were averaged across trials and Gaussian filtered. Mice were then immediately transferred to a surgical station for retrograde tracer injections. For calcium imaging of A1, intrinsic imaging signal was acquired through a chronically implanted window (methods below).

Retrograde tracer injections. Cholera toxin B retrograde tracers (200-300 uL) CTB-555, CTB-647, and CTB-488 were stereotaxically injected in right caudate putamen, right inferior colliculus and left A1, respectively. Mice were perfused ~4 days later.

Histology. Perfused tissue was left in 4% PFA overnight and then cryoprotected in 30% sucrose for at least 24-48 hours. Tissue was frozen and sliced coronally (100 um) on a microtome and mounted on slides with DAPI to label all cells.

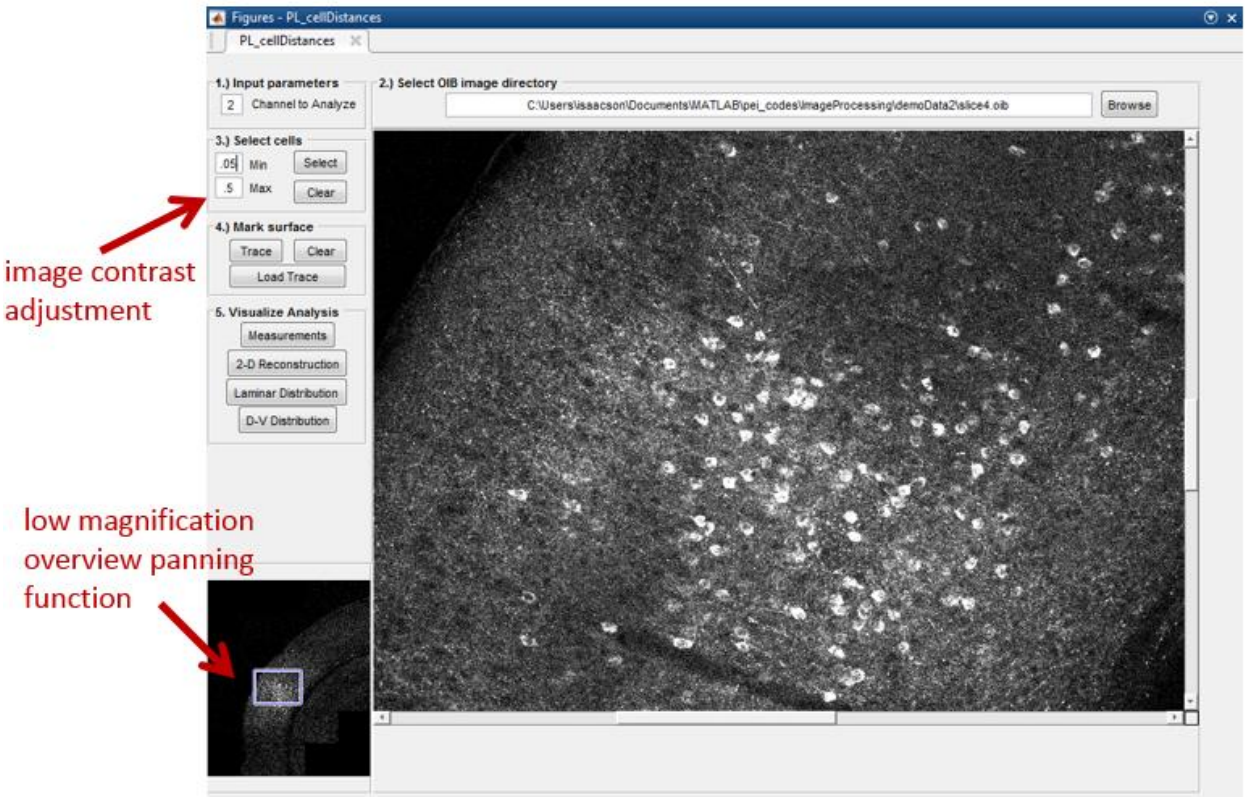

Figure 1.4. Basic functionality of the PL_cellDistances GUI for reconstructing the spatial distribution of neural populations.

Three-dimensional reconstruction of projection neuron populations. A custom MATLAB GUI (PL_cellDistances) was created to quantify the spatial organization of the labeled projection populations. The user begins by manually selecting a channel of interest browsing for an image file (Olympus Fluoview .oib format) to quantify. Once the image is loaded and displayed in the GUI, the user can choose to adjust image contrast (top left, Figure 1.2) and pan around to look at specific regions of interest using a low magnification overview window (bottom left, Figure 1.2).

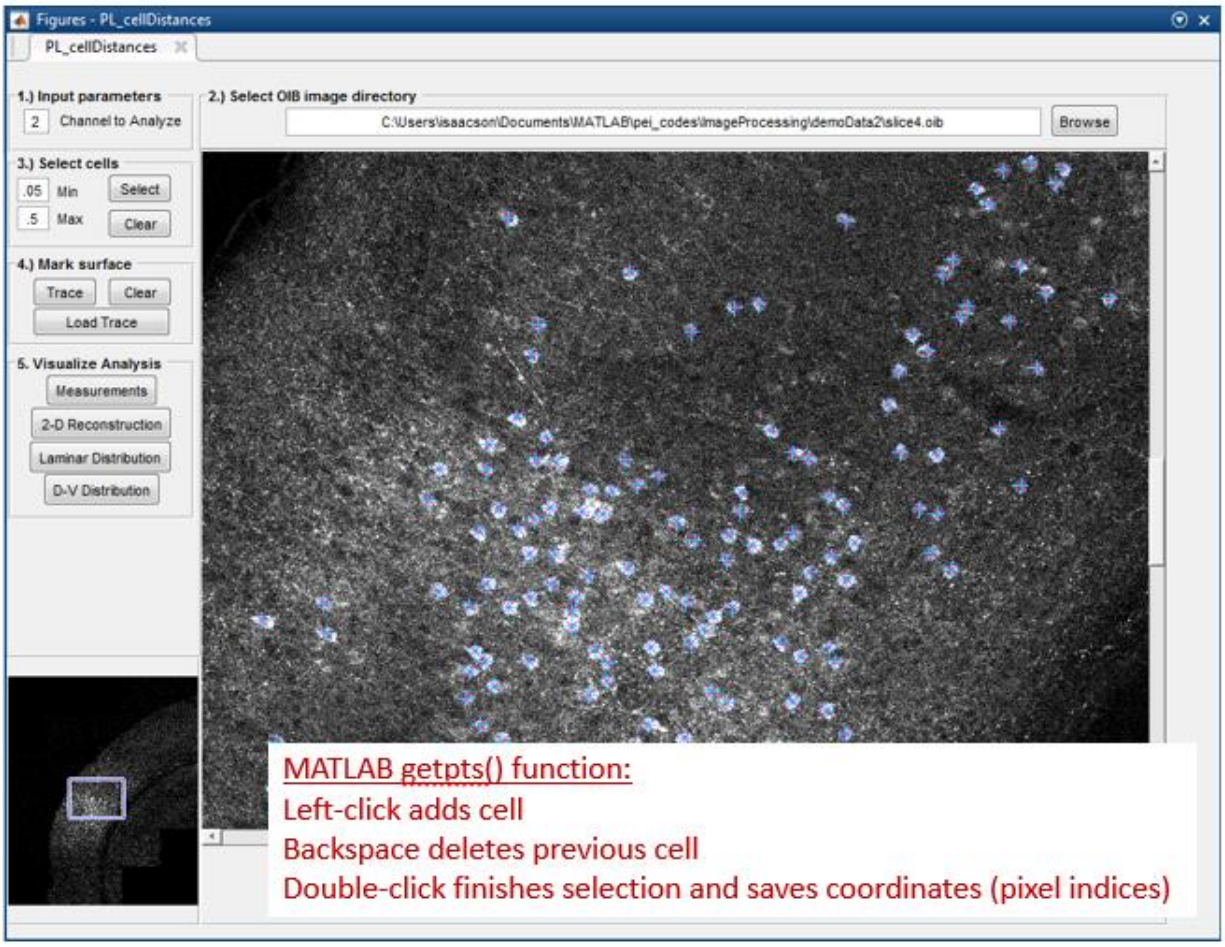

Figure 1.5. Selection of cells in the PL_cellDistances GUI.

To select cells within the image, the user clicks the Select button in the GUI (Figure 1.3). The cursor will then appear as a cross in the main image window to allow the user to place a marker over each cell. Backspace on the keyboard allows for removal of markers in the reverse order with which they were placed, and Enter on the keyboard ends the selection and saves pixel coordinates for each selected cell. The Clear button in the GUI allows the user to reset selection and start over.

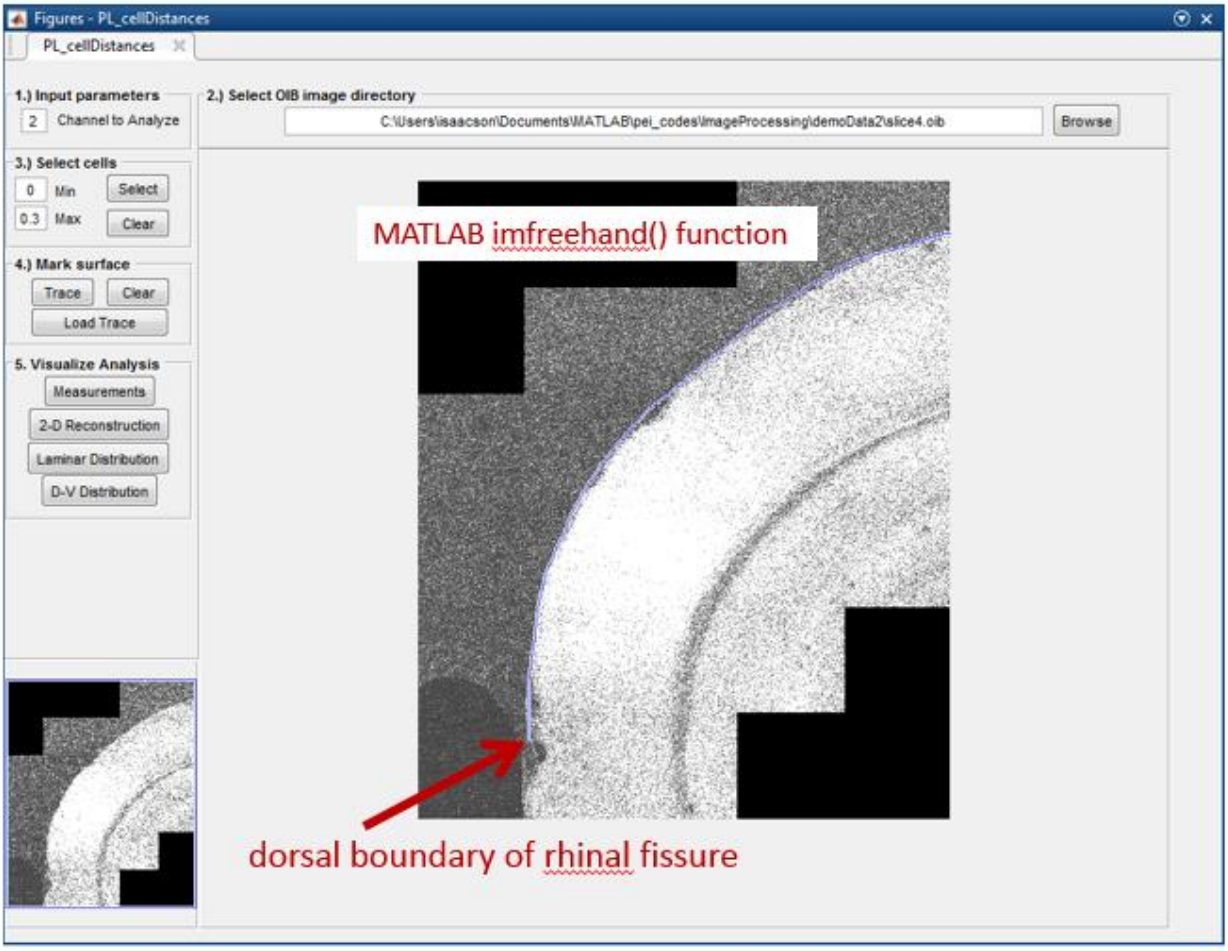

Figure 1.6. Demarcating landmarks in the PL_cellDistances GUI.

Prior to calculating the laminar depth and distance from the rhinal fissure of each selected cell, the cortical tissue surface (pia) and the rhinal fissure must be marked by the user to calibrate each image (Figure 1.4). To draw a curve beginning at the dorsal edge of the rhinal fissure and running along the pia, the user must first click the Trace button in the GUI. Alternatively, the user may load a previously drawn curve by clicking Load Trace in the GUI.

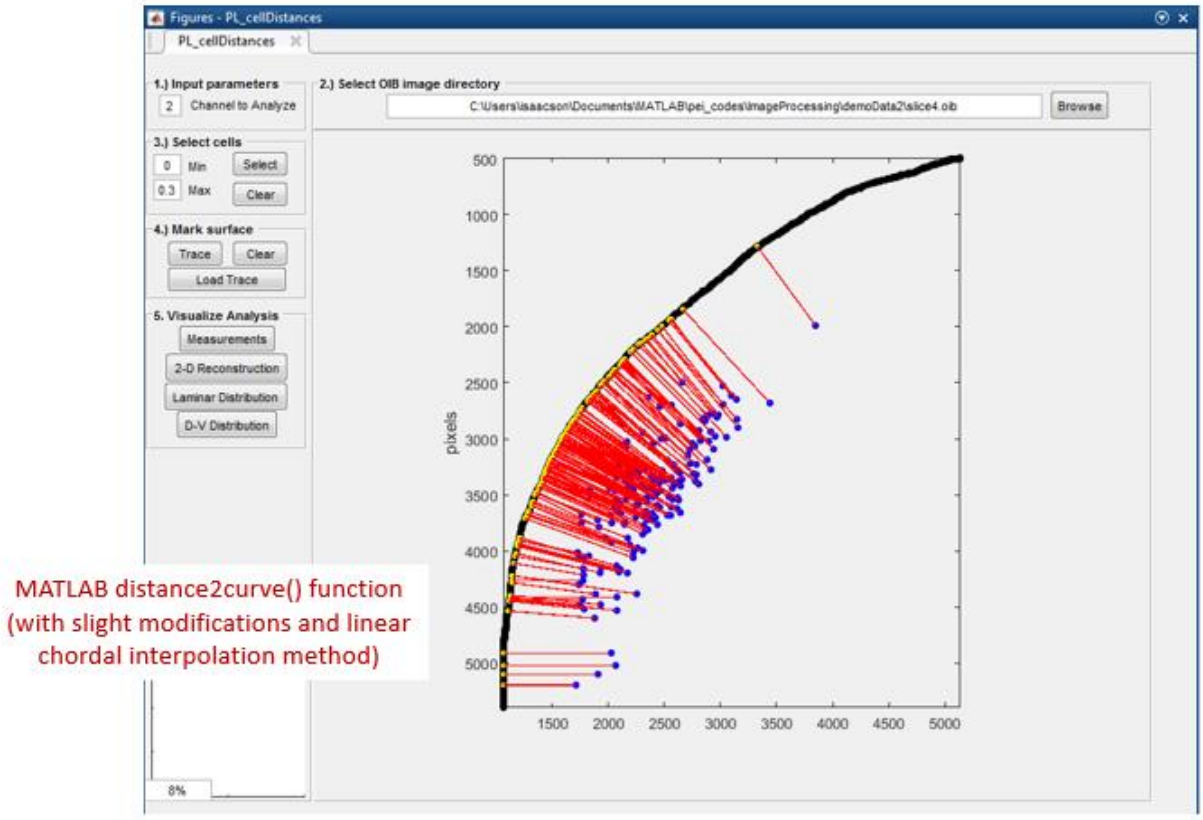

Figure 1.7. Measuring each cell's laminar depth and distance from the rhinal fissure in the PL_cellDistances GUI.

Finally, to generate and save the laminar depth and chordal distance from the rhinal fissure of each cell, the user clicks the Measurements button in the GUI (Figure 1.5). Additional but optional analysis visualizations are available underneath the Measurements button, including two-dimensional reconstruction of cell locations, plotting of laminar distribution of cells, and plotting of dorsoventral distribution of cells.

Quantifying overlap of projection populations. Another custom MATLAB GUI (PL_calculateOverlap) was created and used to quantify the overlap of CTB-expressing cell populations (Figure 1.6). The input to this GUI is a multi-channel .oib (Olympus Fluoview) file. The user can select up to 3 channels simultaneously to visualize the overlap between multiple

cell populations (4th channel is DAPI). The methods for selecting and measuring the spatial coordinates of cells with overlapping tracers is then completed in the same manner as in PL_cellDistances.

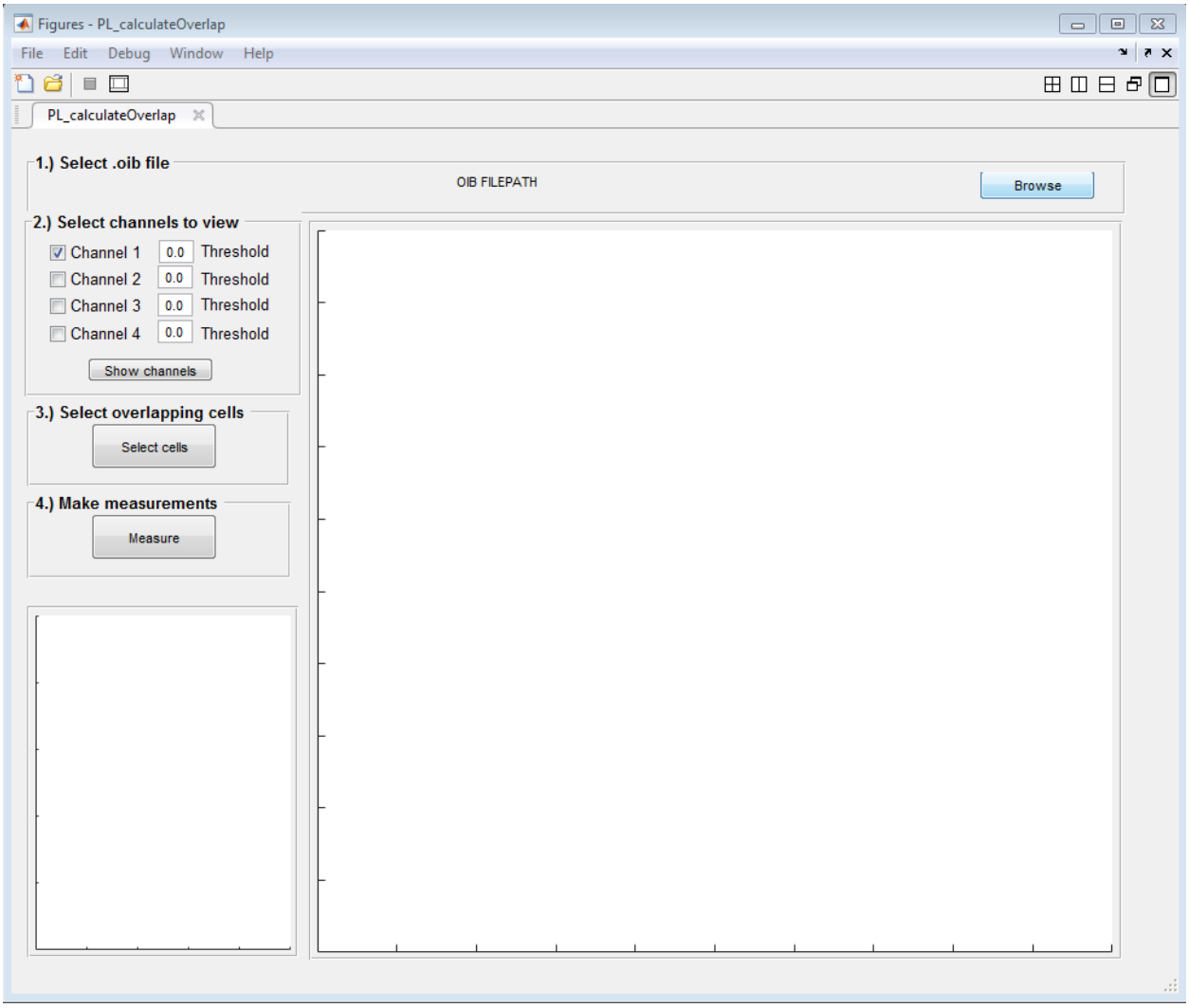

Figure 1.8. Basic functionality of the PL_calculateOverlap GUI for visualizing cells with overlapping retrograde tracer signals.

Sound stimuli. Auditory stimuli were delivered via a free-field electrostatic speaker (ES1; Tucker-Davis Technologies). For intrinsic and calcium imaging, speakers were calibrated over a range of 2-40 kHz to give a flat response (± 1 dB). For in vivo whole-cell recording, speakers were calibrated over a range of 4-60 kHz. Stimuli were delivered to the ear contralateral to imaging or recording. Auditory stimulus delivery was controlled by software

(Dispatcher; http://brodylab.org) running on MATLAB (MathWorks) communicating with a real-time system (RTLinux).

Chronic window implantation. Glass windows for calcium imaging were implanted as described previously (Kato et al., 2015). In summary, mice were anaesthetized with isoflurane and injected with dexamethasone (2 mg/kg) intraperitoneally. A custom stainless steel head-bar was glued to the skull. Muscle overlying the right auditory cortex was removed and a craniotomy (~2 × 3 mm) was made, leaving the dura intact. A glass window was placed over the craniotomy and secured with dental acrylic. Baytril (10 mg/kg) and buprenorphine (0.1 mg/kg) were injected before mice were returned to their home cages.

Two-photon calcium imaging. GCaMP6s was excited at 920 nm (Mai Tai, Newport), and images (512 × 512 pixels covering ~500 × 500 μm) were acquired at 28.4 Hz with a commercial microscope (B-scope, Thorlabs) running Scanimage software using a 16× objective (Nikon). Two-photon imaging fields were aligned with the intrinsic signal imaging fields by comparing blood vessel patterns. Images were acquired from L2/3 (120–250 μm below the surface) at 2X zoom.

Imaging analysis. Lateral motion was corrected by Suite2p phase correlation-based image alignment (Pachitariu et al., 2016). Regions of interest (ROIs) corresponding to visually identifiable cells were detected by Suite2p and manually refined, and pixels within each ROI were averaged to create a fluorescence time series $F_{cell\_measured}(t)$. To correct for neuropil contamination, ring-shaped background ROIs (starting at 2 pixels and ending at 8 pixels from the border of the ROI) were created around each cell ROI. From this background ROI, pixels that contained cell bodies or processes from surrounding cells were excluded. The remaining pixels were averaged to create a background fluorescence time series $F_{background}(t)$. The fluorescence signal of a cell body was estimated as $F(t) = F_{cell\_measured}(t) – 0.9 \times F_{background}(t)$. To ensure robust neuropil subtraction, only cell ROIs that were at least 3% brighter than the background ROIs were included. Sound-evoked responses were measured during one second

tone presentations. Cells were judged as significantly excited (inhibited) if they fulfilled two criteria: 1) dF/F had to exceed a fixed threshold value consecutively for at least 0.5 seconds in more than half of trials. 2) dF/F averaged across trials had to exceed a fixed threshold value consecutively for at least 0.5 seconds. Threshold for excitation (1.9 × standard deviation during baseline period) was determined by receiver operator characteristic (ROC) analysis to yield a 90% true positive rate in receptive field measurements. Since inhibitory responses tend to be small in amplitude, the threshold for inhibition was set as half that for excitation (-0.95 × standard deviation) to increase detection sensitivity. Lifetime sparseness (Rolls and Tovee, 1995; Willmore and Tolhurst, 2001), or *Sp*, was calculated as $(1-\{[\sum_{j=1,N} r_j/N]^2/[\sum_{j=1,N} r^2_j/N]\})/(1-1/N)$, where r_j was the response peak amplitude of the cell to tone *j*, and *N* was the total number of tones. (1 – *Sp)* provides a measure of how much the response probability of a neuron was distributed equally among all tones (non-selective: 1 − *Sp* = 1) versus attributable entirely to one tone (highly selective: 1 − *Sp* = 0).

References

Chen, X., Zhan, H., Kebschull, J.M., Sun, Y.-C., and Zador, A.M. (2018). High-throughput mapping of long-range neuronal projection using in situ sequencing. BioRxiv.

Guo, L., Walker, W.I., Ponvert, N.D., Penix, P.L., and Jaramillo, S. (2018). Stable representation of sounds in the posterior striatum during flexible auditory decisions. Nat. Commun. *9*, 1534.

Kato, H.K., Gillet, S.N., and Isaacson, J.S. (2015). Flexible Sensory Representations in Auditory Cortex Driven by Behavioral Relevance. Neuron *88*, 1007–1039.

Kim, E.J., Juavinett, A.L., Kyubwa, E.M., Jacobs, M.W., and Callaway, E.M. (2015). Three Types of Cortical Layer 5 Neurons That Differ in Brain-wide Connectivity and Function. Neuron *88*, 1253–1267.

LeDoux, J.E., Farb, C.R., and Romanski, L.M. (1991). Overlapping projections to the amygdala and striatum from auditory processing areas of the thalamus and cortex. Neurosci. Lett. *134*, 139–144.

Lur, G., Vinck, M.A., Tang, L., Cardin, J.A., and Higley, M.J. (2016). Projection-Specific Visual Feature Encoding by Layer 5 Cortical Subnetworks. Cell Rep. *14*, 2538–2545.

Pachitariu, M., Stringer, C., Schröder, S., Dipoppa, M., Rossi, L.F., Carandini, M., and Harris, K.D. (2016). Suite2p: beyond 10,000 neurons with standard two-photon microscopy. BioRxiv.

Rolls, E.T., and Tovee, M.J. (1995). Sparseness of the neuronal representation of stimuli in the primate temporal visual cortex. J. Neurophysiol. *73*, 713–726.

Sun, Y.J., Kim, Y.-J., Ibrahim, L.A., Tao, H.W., and Zhang, L.I. (2013). Synaptic Mechanisms Underlying Functional Dichotomy between Intrinsic-Bursting and Regular-Spiking Neurons in Auditory Cortical Layer 5. I. Performed Res. J Neurosci March *20*.

Wang, Q., and Burkhalter, A. (2013). Stream-Related Preferences of Inputs to the Superior Colliculus from Areas of Dorsal and Ventral Streams of Mouse Visual Cortex. J. Neurosci. *33*, 1696–1705.

Willmore, B., and Tolhurst, D.J. (2001). Characterizing the sparseness of neural codes. Network *12*, 255–270.

Xiong, X.R., Liang, F., Zingg, B., Ji, X., Ibrahim, L.A., Tao, H.W., and Zhang, L.I. (2015). Auditory cortex controls sound-driven innate defense behaviour through corticofugal projections to inferior colliculus. Nat. Commun. *6*, 1–12.

Znamenskiy, P., and Zador, A.M. (2013). Corticostriatal neurons in auditory cortex drive decisions during auditory discrimination. Nature *497*, 482–487.

CHAPTER 2: The effects of discriminative auditory fear learning on amygdalocortical sensory representations

Abstract

Sensory representations in the brain are dynamically modulated by changes in behavioral relevance. In many areas of the brain including the auditory thalamus (MG), auditory cortex (AC), and amygdala, electrophysiology studies have revealed enhanced responses to a tone stimulus (CS+) that is conditioned by pairing with an aversive, unconditioned stimulus (US) such as a tail shock. Some studies have also reported a weakening of responses to an emotionally neutral tone stimulus (CS-) concurrent to or instead of enhanced CS+ responses. Within the complex circuitry that is engaged during discriminative auditory fear conditioning (DAFC), the secondary auditory cortex (A2) is uniquely poised as the recipient of direct projections from several areas of the brain that are thought to be required for discriminative fear retrieval: MG, primary auditory cortex (A1), and the lateral amygdala (LA). However, very little is known about what effects DAFC may have on sensory representations in A2 and whether those changes, if any, occur locally or reflect plasticity from upstream regions. To begin addressing this question, we utilized dual-channel, longitudinal calcium imaging of LA projections and A2 somas in awake mouse auditory cortex layer 2/3 before and after DAFC.

Introduction

Investigating the manner in which sensory representations are modulated by behavioral relevance is crucial for understanding how our brains represent the world around us and guide behavioral output. In a process termed habituation, repeated presentations of the same pure tone results in an increase in tone-evoked SOM-mediated inhibition and a decrease in tone-evoked pyramidal cell excitation in primary auditory cortex (A1). Associating detection of the tone with reward (i.e. increasing the behavioral relevance of the stimulus) reverses these effects (Kato et al., 2015). In another related study, mice were presented with randomly interleaved

presentations of two frequency-modulated (FM) tones with distinct carrier frequencies. The first tone remained emotionally neutral (CS-) while each presentation of the second tone (the conditioned stimulus, or CS+) was paired and co-terminated with a tail shock (the unconditioned stimulus, or US). This discriminative auditory fear conditioning (DAFC) paradigm was found to require the auditory cortex (AC) during retrieval and resulted in selective SOM-mediated habituation of pyramidal cell responses to the CS- but not to the CS+ when tested in the absence of paired shocks (Gillet et al., 2018). Thus, an increase in the behavioral relevance of a sound stimulus, regardless of emotional valence, counteracts habituation in A1.

The aforementioned studies employed two-photon calcium imaging of awake mouse A1 and bear the distinct advantage of monitoring the activity of the same cortical neurons at single cell resolution over a period of days. However, it is important to note that the DAFC-related plasticity reported by these calcium imaging experiments differs from the plasticity reported by single unit recording studies, which have primarily tested CS-evoked activity during or immediately after conditioning and lack the ability to monitor the same cells during pre- and post-conditioning recording sessions. In these studies, a selective enhancement of responses to the CS+ is observed in AC as well as in the amygdala, a structure that plays a vital role in emotion processing (Bakin and Weinberger, 1990; Collins and Paré, 2000; Diamond and Weinberger, 1986; Ghosh and Chattarji, 2015; Goosens et al., 2003; Quirk et al., 1997; Repa et al., 2001; Weinberger and Diamond, 1987; Weinberger, 1997, 2004, 2015).

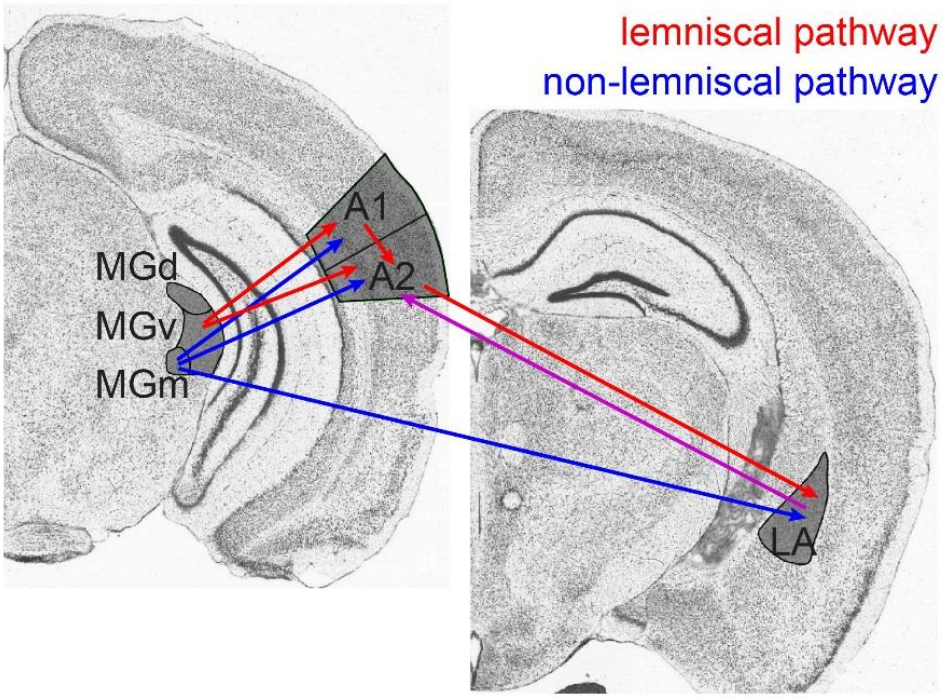

Figure 2.1. Lemnical and non-lemniscal pathways to the lateral amygdala (LA). The lateral amygdala receives information related to auditory fear conditioning indirectly via the lemniscal pathway (red arrows) and directly via the less tonotopic non-lemniscal pathway (blue arrows). In addition to receiving direct inputs from primary auditory cortex (A1) and the auditory thalamus (MG), secondary auditory cortex (A2) receives direct input from LA (purple arrow). MGd – dorsal medial geniculate; MGv – ventral medial geniculate; MGm – medial division of the medial geniculate; A1 – primary auditory cortex; A2 – secondary auditory cortex; LA – lateral amygdala. Hemi coronal slice images acquired from Allen Brain Insitute adult mouse reference atlas.

In fact, the role of the amygdala in auditory fear conditioning has been investigated far more extensively than any other structure thus far. Nevertheless, it has become increasingly apparent that fear memory encoding involves significant contributions from modality-specific thalamic nuclei, sensory cortices, and dorsal medial prefrontal cortex (Herry and Johansen, 2014; LeDoux, 2000; Maren and Quirk, 2004). Despite the complexity of auditory fear memory circuitry (Figure 2.1-2), a combination of tracing, lesioning and electrophysiology studies have pinpointed the lateral amygdala (LA) as the first structure to receive and integrate sensory inputs representing the CS-, CS+, and US (Helmstetter and Bellgowan, 1994; LeDoux, 2000; LeDoux et al., 1990; Maren et al., 2001; Medina et al., 2002; Muller et al., 1997; Wilensky et al.,

1999). Strong evidence for this conclusion is also provided by electrophysiology studies which report that the LA exhibits notably short latencies for associative plasticity within and across conditioning trials (<20 ms from sound onset and within 1-3 trials), and the observed latencies are on par with latencies reported in the auditory thalamus (MG) (Disterhoft and Olds, 1972; Olds et al., 1972; Quirk et al., 1997). On the other hand, conditioning-related response plasticity has been observed at longer latencies in the basolateral amygdala (BLA), central amygdala (CEA), and AC (Diamond and Weinberger, 1986; Li et al., 1996; Maren et al., 1991; Pascoe and Kapp, 1985; Quirk et al., 1997; Uwano et al., 1995). Within these structures, the secondary auditory cortex (A2) appears to play a unique role in the auditory fear pathway, serving as the sole recipient of direct inputs from the LA, MG, and A1 (Antunes and Moita, 2010; Ohga et al., 2018; Yang et al., 2016) (Figure 2.1). Despite the central position of A2 in auditory fear memory circuitry, knowledge about the effects of DAFC on A2 cells and LA cells that specifically project to A2 remains incomplete.

Here, we take advantage of dual channel and longitudinal two-photon calcium imaging in awake mouse A2 to investigate the effects of DAFC on amygdalar and cortical sound representations. Readouts of the autonomic nervous system including freezing behavior, heart rate, and pupil dilation are commonly used to monitor strength of fear memory, and these behaviors are known to be driven by projections from LA to CEA and then from CEA to various brainstem circuits (Davis, 1997; Goosens and Maren, 2001; Koutsikou et al., 2014; Medina et al., 2002) (Figure 2.2). For example, electrical stimulation of the central amygdala results in pupil dilation (Applegate et al., 1983; Davis, 1997; Ursin and Kaada, 1960), presumably via circuitry involving the locus coeruleus (McGinley et al., 2015; Szabadi, 2012). Furthermore, human pupillometry and fMRI studies have revealed a positive correlation between phasic pupil responses and activity in brain regions involved in fear learning, including the amygdala and anterior cingulate cortex (Leuchs et al., 2017). Since our imaging experiments necessitate head-

fixation, we selected pupil dilation as a reliable and non-invasive metric for quantifying strength of DAFC fear memory in this study.

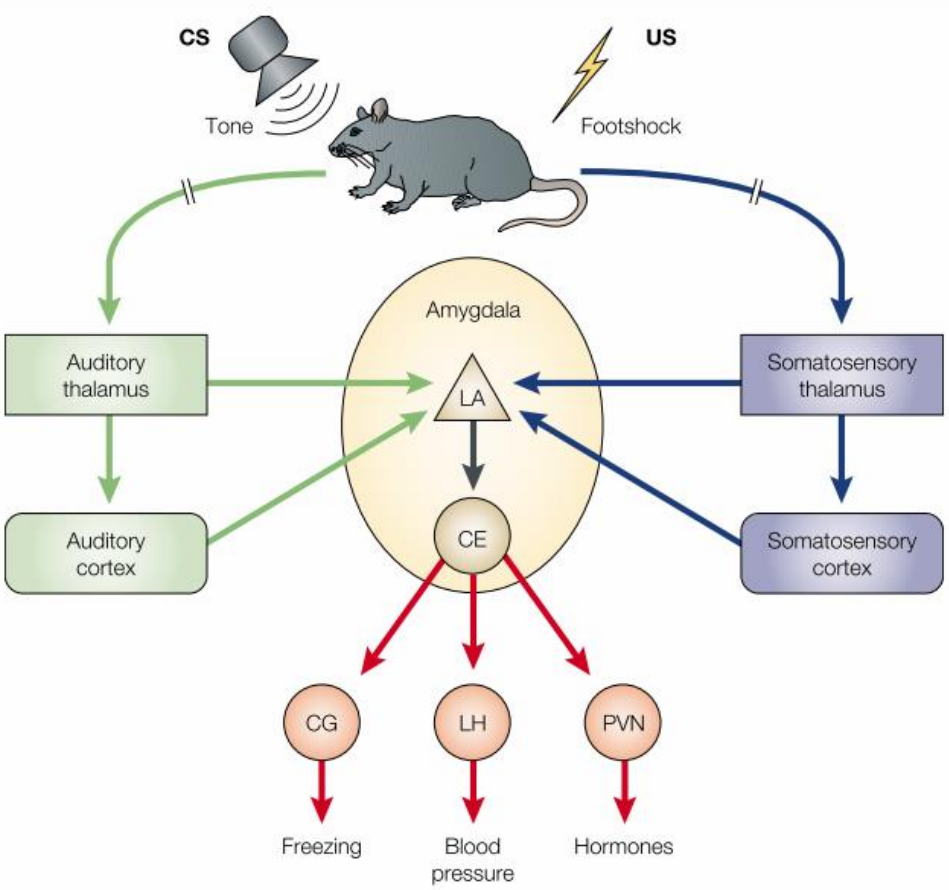

Figure 2.2. Neural circuits engaged during auditory fear conditioning (Medina et al., 2002). CS – conditioned stimulus; US – unconditioned stimulus; LA – lateral amygdala; CE – central amygdala; CG – central grey; LH – lateral hypothalamus; PVN – paraventricular nucleus.

We show that multi-day conditioning results in a selective decrease in response strength and increase in sparseness of representation for the CS-. Concurrently, we observed a selective increase in response strength and decrease in sparseness of representation for the CS+. We also find that this bidirectional associative plasticity in LA largely precedes the development of overt discriminative fear behavior. Furthermore, while the magnitude of pupil dilation and strength of tone-evoked activity were positively correlated throughout our experiments, correlation between pupil dilation and CS+ response strength was consistently weaker than the

correlation between pupil dilation and CS- response strength. Finally, a stronger correlation between pupil dilation and the strength of tone-evoked response strength did not become more apparent during the first retrieval, as would be expected if conditioned pupil dilation were to causally modulate LA CS-evoked activity. Thus, we conclude that any positive correlation in LA activity and pupil dilation cannot possibly be related to fear behavior acquisition and is instead likely to be attributable to general changes in brain state, such as arousal and attention. Taken together, our results suggest that while DAFC-related changes in amygdalocortical activity encode an associative fear memory that may play a large role in the emergence of robust expression of discriminative fear behavior, this plasticity is not sufficient for expression of the behavior itself. The effects of DAFC on local A2 neurons, which integrate direct input from MG, A1, and LA, remain to be determined by further experiments.

Results

In addition to our interest in how DAFC modulates sensory representations in LA neurons that specifically target superficial AC, we were also curious to what degree and on what relative time scale any effects observed in amygdalocortical projections would be reflected in local A2 neurons. To this end, we first injected AAV2.9-Syn-GCaMP6s in LA and waited 2-3 weeks for axonal GCaMP6s expression to begin manifesting in A2. Mice were then anesthesized and underwent a craniotomy and injection of AAV2.1-Syn-jrGECO1a in right AC before implantation of a chronic imaging window (Figure 2.3A, left). GCaMP6s-labeled axons and jrGECO1a-labeled somas in A2 layer 2/3 were visible within 7 days of window implantation (Figure 2.3A, middle); however, mice were handled and habituated to the imaging setup for 8-10 days after surgery before commencing DAFC experiments (Figure 2.3A, right). During imaging, an electrostatic speaker and high-speed camera were located contralateral to the imaging field of view (FOV) for tone presentation and pupillometry, respectively. In the absence of visible light during imaging, pupil dilations are difficult to consistently detect without artificially constricting the pupil to a steady baseline level. For this reason, a 590 nm amber LED optic fiber was located anterior of the imaging FOV and targeted at the animal's left eye to constrict the pupil to approximately 50% of maximum dilation. To block the amber light from reaching the photomultiplier tubes used for acquisition of calcium indicator signals, the cement head cap of the mouse was painted with black nail polish, and an extensive system of blackout curtains was fashioned around the imaging stage.

The speed at which a DAFC-related behavioral response is acquired presumably depends on the complexity and salience of the auditory stimuli as well as the conditioning protocol itself. Nevertheless, the precise relationships between rate of fear acquisition and protocol design factors including sound pressure level, sound duration, sound complexity, and innate behavioral relevance of sounds have not been systematically tested and remain poorly

defined. Furthermore, the aversiveness of the unconditioned stimulus (US), including its strength, duration, and the manner in which it is delivered, can greatly affect learning outcomes (Baldi et al., 2004; Laxmi et al., 2003). In our pilot behavior experiments, we observed that the number of conditioning days required to develop statistically significant, discriminative pupil dilation to the CS- and CS+ varied widely between 1 to 3 days, regardless of whether pure tones, frequency-modulated (FM), or amplitude-modulated (AM) tones were presented (data not shown). However, increasing the shock amplitude above 1 mA did not improve this variability and instead resulted in a notable tendency for mice to generalize fear across both stimuli. This effect was likely, in part, due to retrieval sessions occurring in essentially the same context as conditioning sessions. We would face significant limitations in differentiating the smells, textures, and visual cues of the imaging box as a result of the complex system of blackout curtains used to precisely block amber light from reaching the PMTs while maintaining well-targeted illumination to constrict the pupil. Thus, we elected to proceed with pure tone stimuli paired with 0.5-1 mA tail shocks and accounted for variability in fear acquisition rate by using a DAFC protocol spanning 5 days (4 conditioning sessions).

Individual mice first exhibited significant discriminative pupil dilation to the CS- and CS+ as early as the first retrieval session (1 mouse) and as late as the last retrieval session (1 mouse) (Figure 2.3C1). Overall, 5 of 7 mice achieved significant discriminative behavior during the second retrieval session or earlier (Figure 2.3C2). Daily localization of the same subset of amygdalocortical projections and local A2 neurons is a substantial challenge in longitudinal imaging experiments. We accomplished this robustly and with reasonable confidence by aligning the imaging FOV for all retrieval days to a maximum projection of all images acquired during the first day of the DAFC protocol (Figure 2.3D).

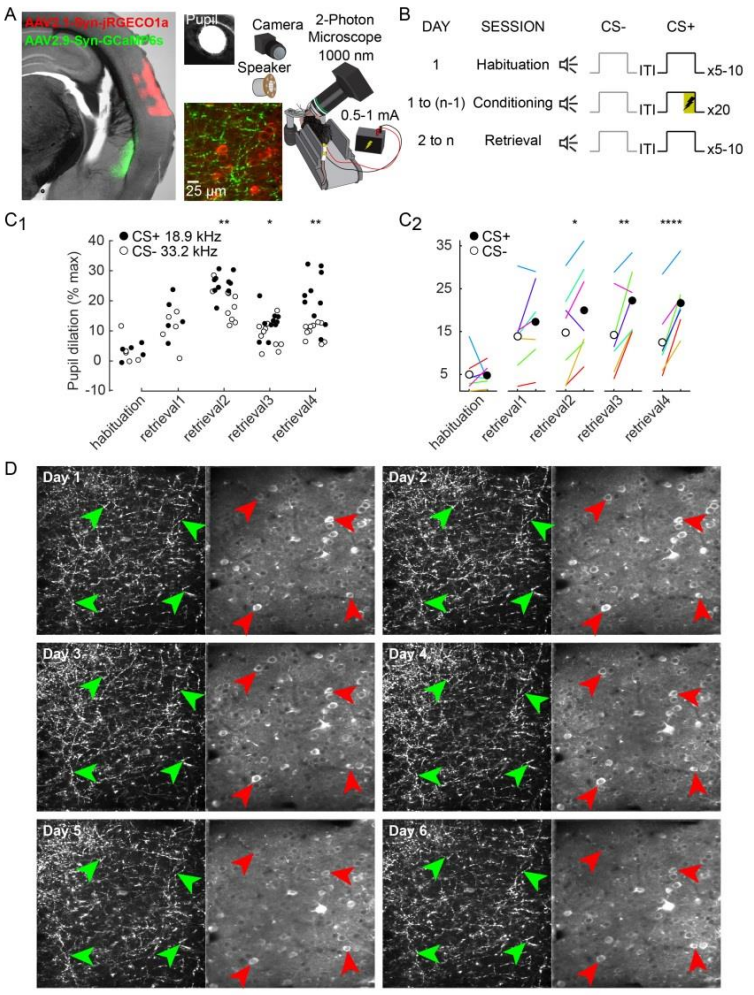

Figure 2.3. Discriminative auditory fear learning is acquired within 1-2 sessions of conditioning. (A) Left, AAV2.9-Syn-GCaMP6s is injected in the lateral amygdala (LA) 2-3 weeks prior to AAV2.1-Syn-jrGECO1a injection in auditory cortex (AC) and chronic window implantation. Right, a high-speed camera and electrostatic speaker are located contralateral to the imaging field of view for pupillometry and tone presentation, respectively. The mouse is head-fixed on a stage and fitted with a tail wire for delivering shocks during all imaging sessions. (B) Each day of imaging begins with either a habituation (day 1) or retrieval session when neither the CS- nor the CS+ are co-terminated with a tail shock, followed by a conditioning session when only the CS+ is co-terminated with a tail shock (C1) Quantification of pupil dilation to CS- and CS+ for a representative experiment in which learned discriminative fear behavior becomes apparent after two conditioning sessions (Mann-Whitney U test; P=0.0058 for retrieval2, P=0.0312 for retrieval3, P=0.0022 for retrieval4). *P<0.05, **P<0.01, ***P<0.001, ****P<0.0001. (C2) Summary quantification of pupil dilation (N=7 mice; CS- and CS+ between 2-40 kHz, spaced 0.54 – 1.08 octaves apart) reveals acquisition discriminative conditioned response after two conditioning sessions (paired t-test). Over multiple sessions of conditioning, the difference in pupil dilation in response to the CS- and CS+ does not significantly increase in magnitude (two-way ANOVA; P=0.01 for stimulus identity, P=0.0002 for session number, p=0.5557 for interaction). (D) Representative maximum projection images of an A2 layer 2/3 calcium imaging field of view confirms successful imaging of the same set of axons and somas over 6 consecutive days of imaging.

The first day of DAFC began with a habituation session in which the CS- and CS+ (5 sec duration, 45±15 sec inter-trial interval) were both presented in randomly interleaved order, for a total of 5 to 10 repetitions and in the absence of the tail shock (US). Pure tone frequencies were selected empirically from a stimulus set of 50 dB pure tones between 2-40 kHz with the goal of maximizing cell responsiveness to both the CS- and CS+ prior to conditioning. For all experiments, the CS- and CS+ were spaced 0.54 to 1.08 octaves apart. After the habituation session, mice underwent their first conditioning session in which the CS- and CS+ were again presented in randomly interleaved order for 20 repetitions, and each CS+ tone was co-terminated with a 2 second duration tail shock. Subsequent days of DAFC began with a retrieval session to test behavioral and cellular responses to the CS- and CS+ in the absence of the US, for a total of 5 to 10 repetitions. Finally, with the exception of the last day of imaging, the retrieval session was always followed by a conditioning session to reinforce fear learning, keeping in mind the possibility that some mice may exhibit slower learning than others (Figure 2.3B).

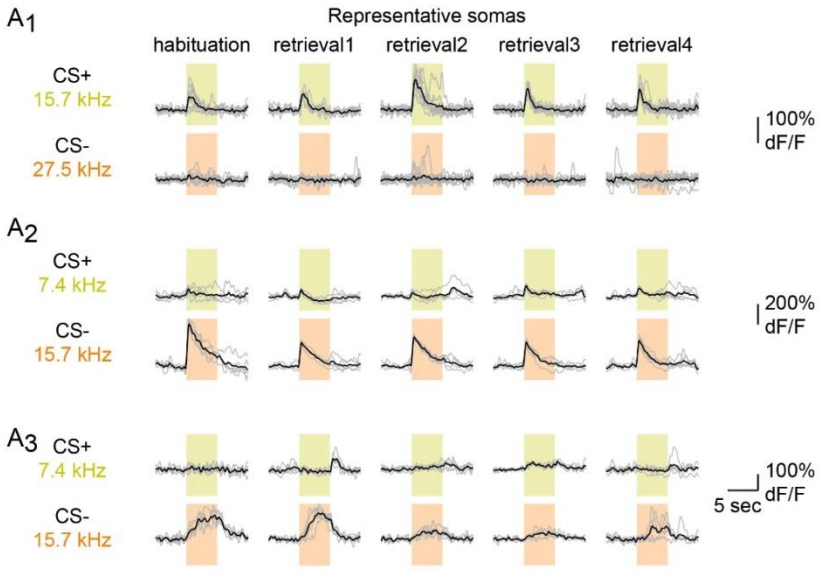

Figure 2.4. Responses of example A2 somas before and after multi-session discriminative auditory fear conditioning. (A1) CS+ responsive soma. (A2-3) CS- responsive somas.

Due to our observation that, on average, significant discriminative pupil dilation manifested only after 2 conditioning sessions, we expected stimulus-specific changes in LA and A2 activity to appear approximately concurrent to the second retrieval session. Interestingly, while overt changes in the activity of some local A2 somas were observed to first appear during the second retrieval session (Figure 2.4), the plasticity observed in amygdalocortical axons seemed to robustly and predominantly appear during the first retrieval session (Figure 2.5). As predicted by previous electrophysiological studies of DAFC-related short-term plasticity, we observed LA axons and A2 somas that exhibited selective increase in responses to the CS+ (Figure 2.4A1, Figure 2.5A3-5), as well as ones that exhibited selective decrease in responses to the CS – (Figure 2.4A2-3, Figure 2.5A1). Additionally, DAFC also appeared to result in suppression of responses to the CS- or CS+ in some cases (Figure 2.5A2, A4).

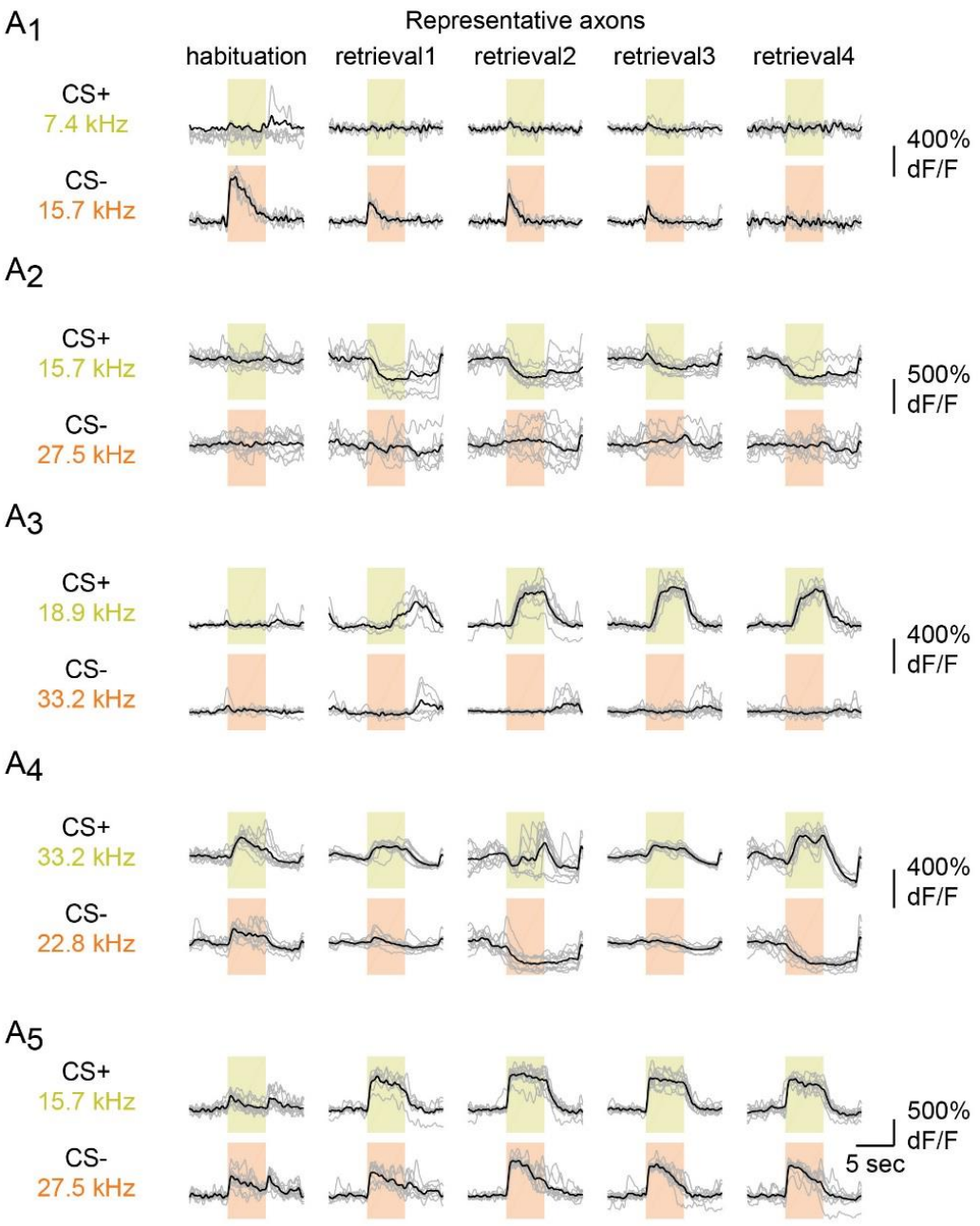

Figure 2.5. Responses of example amygdalocortical axons before and after multi-session discriminative auditory fear conditioning. (A1) CS- responsive axon. (A2) CS+ responsive axon exhibiting suppression during retrieval. (A3) CS+ responsive axon exhibiting gradually stronger and shorter-latency excitation during retrieval. (A4) Axon exhibiting stronger responses to the CS+ and increased suppression to the CS- during retrieval. (A5) Axon exhibiting stronger responses to both the CS- and CS+ during retrieval.

We then quantified z-scored responses in two ways to assess whether DAFC resulted in changes in amygdalocortical activity: integral during the tone period serves as a measure of sustained response strength and peak during the tone period serves as a measure of transient response strength. Due to a low sample size for tone-responsive A2 somas (n = 10 cells), we focused all further analysis on the amygdalocortical axons (n = 867 cells). Despite the broad spectrum of effects observed in individual axons, the overall effect of DAFC on amygdalocortical axon activity is a selective increase in sustained response strength to the CS+ (Figure 2.6A, top right; Figure 2.6B, bottom) and a selective decrease in transient response strength to the CS- (Figure 2.6B, top). The increase in CS+ sustained response strength relative to that of habituation was statistically significant (two-way ANOVA; $P<0.0001$ for stimulus identity; $P=0.025$ for session number; $P=0.0735$ for interaction) after one conditioning session, while the decrease in CS- transient response strength was statistically significant (two-way ANOVA; $P<0.0001$ for stimulus identity; $P=0.0891$ for session number; $P=0.0593$ for interaction) after three conditioning sessions. Taken together, DAFC results in selective, bidirectional changes in tone-evoked response strength in amygdalocortical projections, with CS+ associative plasticity occurring relatively faster than CS- associative plasticity.

Next, we explored the overall sparseness of CS- and CS+ amygdalocortical representations and observed a significant interaction effect between stimulus identity and session number (two-way ANOVA; $P=0.0497$), indicating that the divergence in sparseness of CS- and CS+ representations varied through multiple days of conditioning. Finally, to determine if the observed changes in response strength and sparseness of representations could contribute to improved discrimination between the CS- and CS+, we measured % of cells with significantly different CS- and CS+ responses and standardized Euclidean distance between CS- and CS+ responses during habituation and each retrieval session (Figure 2.6D). As expected, the discriminability of population CS- and CS+ responses increased with conditioning (Friedman's ANOVA, Discriminating cells $P=0.05$, Std. Euclidean distance $P=0.0136$).

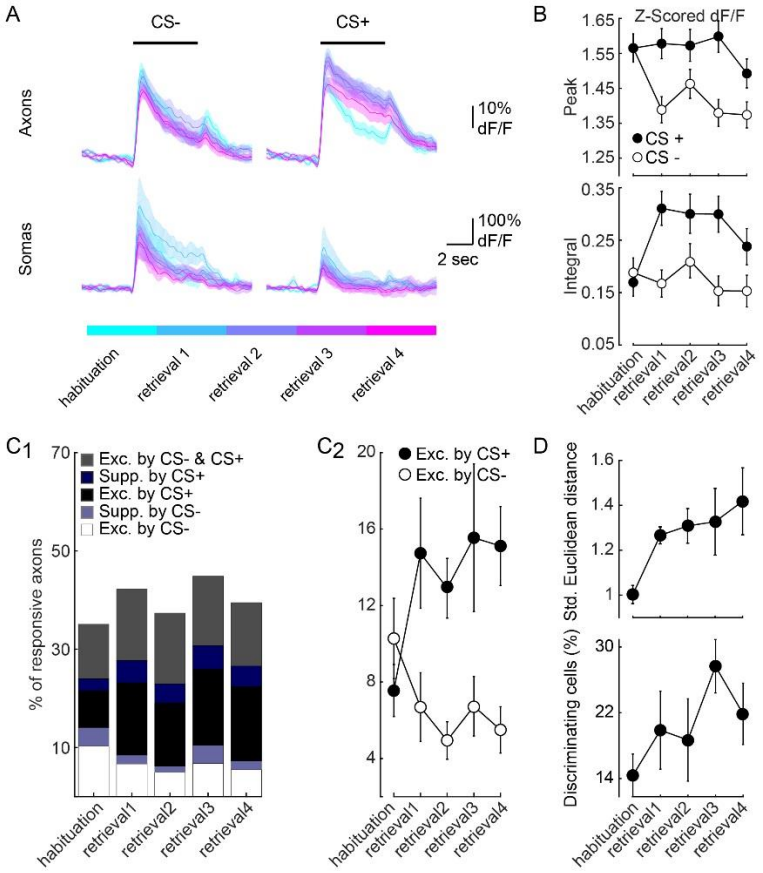

Figure 2.6. DAFC mediates bidirectional effects on CS- and CS+ response strength and sparseness of representations. (A) Mean raw traces of LA axon (top) and A2 soma (bottom) responses to the CS- and CS+ during habituation and retrieval sessions. Cells deemed to be responsive to either the CS- or the CS+ (Wilcoxin rank sum test, see Experimental Procedures) during any habituation or retrieval session were included in this analysis. (B) Z-scored traces were quantified by peak during the tone period as a measure of transient response strength, and by integral during the tone period as a measure of sustained response strength. CS+ sustained response strength increased relative to that of habituation (two-way ANOVA; $P<0.0001$ for stimulus identity; $P=0.025$ for session number; $P=0.0735$ for interaction) during the first retrieval session (post-hoc multiple comparisons; $p=0.0474$), while CS- transient response strength decreased (two-way ANOVA; $P<0.0001$ for stimulus identity; $P=0.0891$ for session number; $P=0.0593$ for interaction) during the third (post-hoc multiple comparisons; $P=0.0449$) and fourth (post-hoc multiple comparisons; $P=0.033$) retrieval sessions. (C1) Major categories of tone-responsive axons include those that are excited by only the CS-, only the CS+, or both, and those that are suppressed by only the CS- or only the CS+. (C2) Sparseness of CS- and CS+ representations become increasingly divergent with DAFC (two-way ANOVA; $P<0.0001$ for stimulus identity; $P=0.8015$ for session number; $P=0.0497$ for interaction). (D) Top, standardized Euclidean distance increases (Friedman's ANOVA; $P=0.0136$) with DAFC. Bottom, the %age of tone-responsive cells with significantly different responses to the CS- and CS+ increases with conditioning (Friedman's ANOVA, $P=0.05$).

To assess whether DAFC also induced short-term plasticity in amygdalocortical cells, we evaluated the average CS- and CS+ responses during early trials (first 5 of 20 presentations) compared to late trials (last 5 of 20 presentations) of the first conditioning session (Figure 2.7). Onset-locked responses to the CS- and CS+ did not appear to change significantly between these time frames. Interestingly, offset-locked CS- responses exhibited a tendency to decrease in magnitude while offset-locked CS+ responses exhibited a tendency to increase in magnitude.

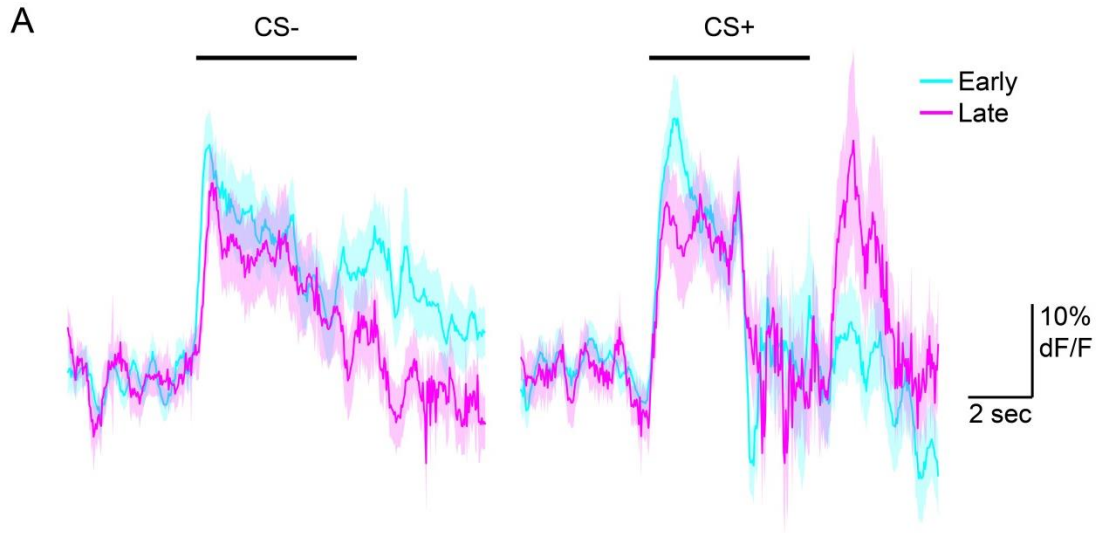

Figure 2.7. Amygdalocortical tone onset responses are not significantly different early in the first conditioning session relative to late in the session. (A) For each axon, each of the first 5 responses to the CS- and CS+ were averaged together and compared to the average waveform of the last 5 responses to the CS- and CS+.

Lastly, we wondered how closely amygdalocortical response strength might correlate with pupil dilation on a trial-by-trial basis, given our intriguing observations that enhancement of CS+ response strength precedes significant discriminative pupil dilation by at least 24 hours. During the first retrieval, CS+ response strength increased and pupil dilations became apparent in response to both the CS- and CS+. If response strength and magnitude of pupil dilation were to form any sort of causal relationship, we would expect correlation between the two to increase significantly after the first conditioning session. In fact, neither correlation between magnitude of pupil dilation and CS- response strength nor correlation between magnitude of pupil dilation and

CS+ response strength increased between habituation and the first retrieval (Figure 2.8). Additionally, the correlation between pupil dilation and CS+ response strength was consistently weaker than the correlation between pupil dilation and CS- response strength. Taken together, these results confirm dissociation of DAFC-related LA plasticity and conditioned fear behavior, and the overall positive correlation between response strength and pupil dilation is likely due to general changes in arousal or attention throughout the conditioning protocol.

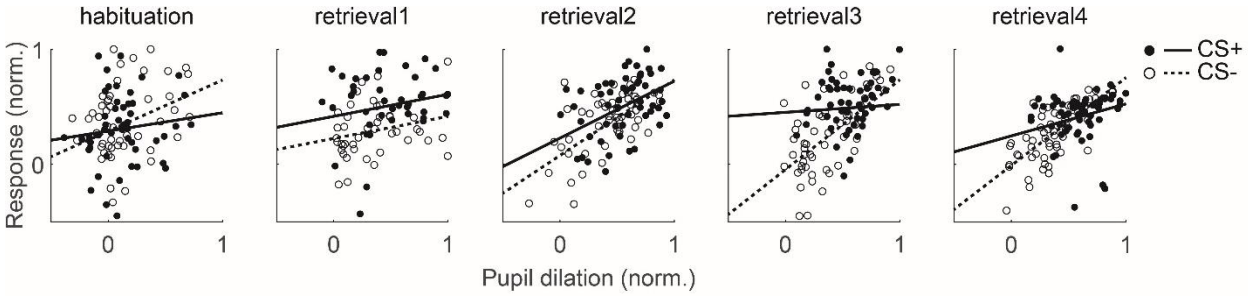

Figure 2.8. Amygdalocortical response strength and magnitude of pupil dilation are positively correlated. Each data point is the population mean sustained response strength during each CS- or CS+ trial (n=867 cells; N = 7 mice). Development of conditioned pupil dilations after the first conditioning session does not appear to significantly increase correlation between CS- and CS+ response strength and pupil dilation (retrieval1). Conversely, development of stronger CS+ responses after the first conditioning session does not significantly increase correlation between CS+ response strength and pupil dilation (retrieval1). Finally, correlation between CS+ response strength and pupil dilation appears consistently weaker than the correlation between CS- response strength and pupil dilation. Thus, no causal relationship is likely to exist between amygdalocortical activity and pupil dilation; however the observed positive correlation during all imaging sessions is likely attributable to general changes in arousal and attention.

Discussion

By tracking the tone-evoked activity of the same subset of A1 layer 2/3 amygdalocortical axons before and after DAFC, we found that responses to the CS+ became more sustained while responses to the CS- weakened. Additionally the sparseness of CS+ representation decreased while the sparseness of CS- representation increased after conditioning. Thus, DAFC results in significant improvement to the discriminability between amygdalocortical CS- and CS+ representations. To the best of our knowledge, our findings are novel and are the first report of selective and bidirectional plasticity in LA to AC projections after DAFC. However, our results are also entirely consistent with the DAFC-related effects reported from single unit recordings in adult cats (Collins and Paré, 2000). This electrophysiology study is comparable to ours in terms of multi-day DAFC protocol design and monitoring of activity in LA over several days; however, there are several significant factors that distinguish the impact of their results from those reported here. First, the sample size of the unit recording study is relatively small (72 cells from 4 animals). Second, it is impossible to discern the downstream structure or structures within the auditory fear pathway that the recorded cells project to. Finally, as is true with all extracellular recording studies, the subset of cells recorded during each retrieval session are highly unlikely to be the same across each day of recordings.

An interesting aspect of our findings is that the DAFC-related changes in LA activity precede the emergence of overt discriminative fear behavior by roughly one conditioning day. While this dissociation between conditioned behavior and conditioning-related LA plasticity is surprising, several previous studies have reported similar findings, albeit on shorter timescales. In one electrophysiology study, an increase in LA responses to the CS+ was observed within just a few pairings of CS with US, but the conditioned freezing response did not emerge until several trials later (Repa et al., 2001). Additionally, some LA neurons maintained enhanced firing to the CS+ after extinction of the fear response. Conditioning-related response plasticity in

secondary auditory cortex of adult cats also precedes the expression of conditioned pupil dilation by many trials (Diamond and Weinberger, 1986). Finally, an impressive and comprehensive unit recording study in rats provides compelling evidence that the LA stores a bonafide CS-US associative fear memory despite complete dissociation from conditioned behavioral responses (Goosens et al., 2003). In this study, rats underwent DAFC as well as contextual fear conditioning before testing in either a neutral context or the conditioned context. If post-conditioning enhancement of CS+ responses is simply a non-associative result of conditioned fear behavior expression rather than a specific association between the CS and the US, then CS- responses would be enhanced when rats are tested for retrieval in the conditioned context. On the contrary, the expression of conditioned fear behavior did not result in enhancement of CS- responses. Furthermore, reversible pharmacological inhibition of CEA eliminated conditioned freezing behavior without affecting post-DAFC enhancement of CS+ responses. Thus, expression of conditioned fear behavior is not necessary or sufficient for inducing an enhancement in LA CS+ responses. In conclusion, our findings are consistent with an existing model which proposes that the LA is a primary site of discriminative fear memory storage and may play a significant role in the subsequent emergence of conditioned fear behavior.

Our next experiments will be aimed at determining whether the dissociation we observed between expression of discriminative fear behavior and conditioning-related plasticity in LA is reflected in the activity of local A2 layer 2/3 neurons, where direct inputs from A1, MG, and LA are integrated. Based on our preliminary findings, we would conclude that LA projections to A2 are unlikely to innervate CEA and drive expression of fear behavior directly. However, the fact that optogenetic silencing of LA to A2 projections blocks retrieval of non-discriminative (no CS- included in protocol) auditory fear memory (Yang et al., 2016) suggests that information transfer along this pathway may also be required for retrieval of DAFC fear memory. Additionally, induction of long-term potentiation (LTP) in A2 to LA projections that carry CS+ information is

sufficient for inducing conditioned fear behavior, and de-potentiation of the same connections impairs memory recall (Kim and Cho, 2017; Nabavi et al., 2014). Taken together, we imagine a model of DAFC circuitry in which A2 is a crucial driver of conditioned fear behavior expression through discriminability in the activity of its direct projections to LA. In this model, LA input to A2 is a necessary complement to the CS- and CS+ representations encoded by MG and A1, especially because DAFC does not seem to result in enhancement of CS+ responses in A1 (Gillet et al., 2018). In order to test this proposed model, we plan to combine longitudinal calcium imaging with optogenetic manipulations during retrieval to investigate how DAFC affects sensory representations in A2 layer 2/3 neurons and whether those changes are encoded locally or are inherited from specific upstream regions.

Experimental Procedures

Animals. Mice between 8 and 16 weeks of age of both genders were used for all experiments. Mice were acquired from Jackson Laboratories (C57BL/6 (Jax: 000664)) and housed in a room with a 12:12 reversed light cycle. Experiments were performed during the dark period. Mice had no prior history of experimental procedures that could affect the results. All procedures were in accordance with protocols approved by the UCSD Institutional Animal Care and Use Committee and guidelines of the National Institute of Health.

Amygdala viral Injection. Three weeks prior to chronic window implantation, mice were stereotaxically injected in right lateral amygdala (2.1 mm behind bregma, 4.35 mm right of the midline, and 4.5 mm deep) with 200 uL of AAV2.9-Syn-GCaMP6s (UPenn Vector Core) diluted 1:40 with sterile PBS, at a rate of 25 nL/min. The surgical site was sutured and mice were returned to home cages for recovery.

AC viral injection and chronic window implantation. Mice were anaesthetized with isoflurane and injected with dexamethasone (2 mg/kg) intraperitoneally. A custom stainless steel head-bar was glued to the skull. Muscle overlying the right auditory cortex was removed and a craniotomy (~2 × 3 mm) was made, leaving the dura intact. At each of 10-15 contiguous locations 275 um below the pial surface, 30 nL of AAV2.1-Syn-jRGECO1a (Addgene) virus was injected in at a rate of 10 nL/min. A glass window was placed over the craniotomy, sealed with Vetbond, and secured with dental acrylic. Baytril (10 mg/kg) and buprenorphine (0.1 mg/kg) were injected before mice were returned to their home cages for recovery.

Mouse handling and habituation. Mice were handled for 5 minutes daily for the first 3 days following window implantation. Then, mice were habituation to head fixation and a tail wire under a two-photon microscope for 2 hours a day for 5-7 days.

Intrinsic signal imaging. Intrinsic signal imaging was performed through chronic windows 1-3 days before calcium imaging to locate A2. Images were acquired using a tandem lens macroscope and 12 bit, CCD camera (CCD-1300QF, VDS Vosskühler). were acquired

using a tandem lens macroscope and 12 bit, CCD camera (CCD-1300QF, VDS Vosskühler). Mice were anesthetized with isoflurane. Images of surface vasculature through the chronically implanted window were acquired using green LED illumination (530 nm) and intrinsic signals were recorded (27 Hz) using red illumination (615 nm). Each trial consisted of a 1s baseline followed by a 1 s sound stimulus (70 dB pure tone with a frequency of 3, 10, or 30 kHz, 10-20 trials per frequency) and a 30 s inter-trial interval. Images of reflectance were acquired at 1024 X 1024 pixels (covering ~2.1 x 2.1 mm) and downsampled to 512 x 512 pixels by interpolation. Images during the response period (0.5-2 s from the sound onset) were averaged and divided by the average image during the baseline. Images were averaged across trials and Gaussian filtered.

Discriminative auditory fear conditioning. Mice were head-fixed on a stage and fitted with a tail wire for delivering shock. Auditory stimuli were delivered via a free-field electrostatic speaker (ES1: Tucker-Davis Technologies). Stimuli were delivered to the ear contralateral to imaging or recording. Auditory stimulus and tail shock delivery was controlled by software (BControl; http://brodylab.org) running on MATLAB (MathWorks) communicating with a real-time system (RTLinux). Mice were presented with two 5-s pure tones, 0.54-1.08 octave apart. Tones (50 dB) were presented from a calibrated, free-field speaker (ES- 1, TDT) positioned approximately 5 cm from the left ear. An inter-trial interval (ITI) of 30–60 s (15 s jitter) separated tone presentations. During conditioning sessions, mice were given a 2 s tail shock (0.5-1 mA) that co-terminated with the presentation of one of the two tones (CS+).

***In vivo* two-photon calcium imaging.** Calcium imaging was performed within 2-3 weeks following chronic window implantation. Two-photon imaging fields were aligned with the intrinsic signal imaging fields by comparing blood vessel patterns. GCaMP6s and jRGECO1a were excited at 1000 nm (Insight X3, Spectra Physics), and images (512 × 512 pixels covering ~500 × 500 μm) were acquired at 30 Hz with a commercial microscope (B-scope, Thorlabs)

running Scanimage 5 software using a 16× objective (Nikon). Images were acquired from L2/3 (120–250 μm below the surface) at 4X zoom.

Imaging analysis. Image registration, ROI detection and refinement, data pre-processing, and detection of significant sound-evoked excitation and suppression was completed using the MATLAB Suite2P/Pei2P pipeline as described in Chapter 4. Axon boutons with a cross-correlation value greater than 0.6 were assumed to be from the same axon and were analyzed as such. The cross-correlation threshold was identified empirically through visualization of boutons clustered with a wide range of correlation thresholds. Raw dF/F traces were z-scored prior to any further analysis. For each DAFC imaging session, the pairwise standardized Euclidean distance between the cells' mean responses (integral dF/F) to the CS- and their mean responses to the CS+ was measured using the MATLAB function pdist2() and averaged together. Cells categorized as "discriminating" were ones which exhibited significantly different CS- and CS+ responses (Wilcoxin signed rank test $P<0.01$ for >80% of time points in at least one 0.5 s window across trials during presentation of CS- or CS+).

Pupillometry. The eye contralateral to imaging or recording was monitored via a compact, high-speed camera (BFLY-U3-05S2M-CS, Point Grey) with 50 mm fixed focal lens (M5018-MP2, Computar). Pupil measurements were acquired via the open-source software Bonsai (bonsai-rx.org).

Analysis of pupil data. Raw pupil diameter was smoothed using a moving average filter over a window of 1 sec, then normalized to the maximum value during a given imaging session or series of recordings from the same mouse.

Histology. Perfused tissue was left in 4% PFA overnight and then cryoprotected in 30% sucrose for at least 24-48 hours. Tissue was frozen and sliced coronally (100 um) on a microtome and mounted on slides with DAPI to label all cells.

Quantification and statistics. All data are presented as mean ± SEM. Statistically significant differences between conditions were determined using standard parametric or

nonparametric tests in MATLAB. All n values refer to the number of cells except when explicitly stated that the n is referring to the number of mice. Experiments were not performed blind. Sample sizes were not predetermined by statistical methods, but were based on those commonly used in the field.

Data and software availability. The custom MATLAB code will be made available upon reasonable request.

References

Antunes, R., and Moita, M.A. (2010). Discriminative Auditory Fear Learning Requires Both Tuned and Nontuned Auditory Pathways to the Amygdala. J. Neurosci. *30*, 9782–9787.

Applegate, C.D., Kapp, B.S., Underwood, M.D., and McNall, C.L. (1983). Autonomic and somatomotor effects of amygdala central N. stimulation in awake rabbits. Physiol. Behav. *31*, 353–360.

Bakin, J.S., and Weinberger, N.M. (1990). Classical conditioning induces CS-specific receptive field plasticity in the auditory cortex of the guinea pig.

Baldi, E., Lorenzini, C.A., and Bucherelli, C. (2004). Footshock intensity and generalization in contextual and auditory-cued fear conditioning in the rat. Neurobiol. Learn. Mem. *81*, 162–166.

Collins, D.R., and Paré, D. (2000). Differential fear conditioning induces reciprocal changes in the sensory responses of lateral amygdala neurons to the CS(+) and CS(-). Learn. Mem. *7*, 97–103.

Davis, M. (1997). The Role of the Amygdala.

Diamond, D.M., and Weinberger, N.M. (1986). Classical conditioning rapidly induces specific changes in frequency receptive fields of single neurons in secondary and ventral ectosylvian auditory cortical fields. Brain Res. *372*, 357–360.

Disterhoft, J.F., and Olds, J. (1972). Differential development of conditioned unit changes in thalamus and cortex of rat. J. Neurophysiol. *35*, 665–679.

Ghosh, S., and Chattarji, S. (2015). Neuronal encoding of the switch from specific to generalized fear. Nat. Neurosci. *18*, 112–120.

Gillet, S.N., Kato, H.K., Justen, M.A., Lai, M., and Isaacson, J.S. (2018). Fear Learning Regulates Cortical Sensory Representations by Suppressing Habituation. Front. Neural Circuits *11*.

Goosens, K.A., and Maren, S. (2001). Contextual and Auditory Fear Conditioning are Mediated by the Lateral, Basal, and Central Amygdaloid Nuclei in Rats.

Goosens, K.A., Hobin, J.A., and Maren, S. (2003). Auditory-evoked spike firing in the lateral amygdala and Pavlovian fear conditioning: mnemonic code or fear bias? Neuron *40*, 1013–1022.

Helmstetter, F.J., and Bellgowan, P.S. (1994). Effects of muscimol applied to the basolateral amygdala on acquisition and expression of contextual fear conditioning in rats. Behav. Neurosci. *108*, 1005–1009.

Herry, C., and Johansen, J.P. (2014). Encoding of fear learning and memory in distributed neuronal circuits. Nat. Neurosci. *17*, 1644–1654.

Kato, H.K., Gillet, S.N., and Isaacson, J.S. (2015). Flexible Sensory Representations in Auditory Cortex Driven by Behavioral Relevance. Neuron *88*, 1007–1039.

Kim, W. Bin, and Cho, J.-H. (2017). Encoding of Discriminative Fear Memory by Input-Specific LTP in the Amygdala. Neuron *95*, 1129-1146.e5.

Koutsikou, S., Crook, J.J., Earl, E. V, Leith, J.L., Watson, T.C., Lumb, B.M., and Apps, R. (2014). Neural substrates underlying fear-evoked freezing: the periaqueductal grey-cerebellar link. J. Physiol. *592*, 2197–2213.

Laxmi, T.R., Stork, O., and Pape, H.-C. (2003). Generalisation of conditioned fear and its behavioural expression in mice. Behav. Brain Res. *145*, 89–98.

LeDoux, J.E. (2000). Emotion Circuits in the Brain. Annu. Rev. Neurosci. *23*, 155–184.

LeDoux, J.E., Cicchetti, P., Xagoraris, A., and Romanski, L.M. (1990). The lateral amygdaloid nucleus: sensory interface of the amygdala in fear conditioning. J. Neurosci. *10*, 1062–1069.

Leuchs, L., Schneider, M., Czisch, M., and Spoormaker, V.I. (2017). Neural correlates of pupil dilation during human fear learning. Neuroimage *147*, 186–197.

Li, X.F., Stutzmann, G.E., and Ledoux, J.E. (1996). Convergent but Temporally Separated Inputs to Lateral Amygdala Neurons from the Auditory Thalamus and Auditory Cortex Use Different Postsynaptic Receptors: In Vivo Intracellular and Extracellular Recordings in Fear Conditioning Pathways.

Maren, S., and Quirk, G.J. (2004). Neuronal signalling of fear memory. Nat. Rev. Neurosci. *5*, 844–852.

Maren, S., Poremba, A., and Gabriel, M. (1991). Basolateral amygdaloid multi-unit neuronal correlates of discriminative avoidance learning in rabbits. Brain Res. *549*, 311–316.

Maren, S., Yap, S.A., and Goosens, K.A. (2001). The amygdala is essential for the development of neuronal plasticity in the medial geniculate nucleus during auditory fear conditioning in rats. J. Neurosci. *21*, RC135.

McGinley, M.J., Vinck, M., Reimer, J., Batista-Brito, R., Zagha, E., Cadwell, C.R., Tolias, A.S., Cardin, J.A., and McCormick, D.A. (2015). Waking State: Rapid Variations Modulate Neural and Behavioral Responses. Neuron *87*, 1143–1161.

Medina, J.F., Christopher Repa, J., Mauk, M.D., and LeDoux, J.E. (2002). Parallels between cerebellum- and amygdala-dependent conditioning. Nat. Rev. Neurosci. *3*, 122–131.

Muller, J., Corodimas, K.P., Fridel, Z., and LeDoux, J.E. (1997). Functional inactivation of the lateral and basal nuclei of the amygdala by muscimol infusion prevents fear conditioning to an explicit conditioned stimulus and to contextual stimuli. Behav. Neurosci. *111*, 683–691.

Nabavi, S., Fox, R., Proulx, C.D., Lin, J.Y., Tsien, R.Y., and Malinow, R. (2014). Engineering a memory with LTD and LTP. Nature *511*, 348–352.

Ohga, S., Tsukano, H., Horie, M., Terashima, H., Nishio, N., Kubota, Y., Takahashi, K., Hishida, R., Takebayashi, H., and Shibuki, K. (2018). Direct Relay Pathways from Lemniscal Auditory Thalamus to Secondary Auditory Field in Mice. Cereb. Cortex *28*, 4424–4439.

Olds, J., Disterhoft, J.F., Segal, M., Kornblith, C.L., and Hirsh, R. (1972). Learning centers of rat brain mapped by measuring latencies of conditioned unit responses. J. Neurophysiol. *35*, 202–219.

Pascoe, J.P., and Kapp, B.S. (1985). Electrophysiological characteristics of amygdaloid central nucleus neurons during Pavlovian fear conditioning in the rabbit. Behav. Brain Res. *16*, 117–133.

Quirk, G.J., Armony, J.L., and LeDoux, J.E. (1997). Fear conditioning enhances different temporal components of tone-evoked spike trains in auditory cortex and lateral amygdala. Neuron *19*, 613–624.

Repa, J.C., Muller, J., Apergis, J., Desrochers, T.M., Zhou, Y., and LeDoux, J.E. (2001). Two different lateral amygdala cell populations contribute to the initiation and storage of memory. Nat. Neurosci. *4*, 724–731.

Szabadi, E. (2012). Modulation of physiological reflexes by pain: role of the locus coeruleus. Front. Integr. Neurosci. *6*, 94.

Ursin, H., and Kaada, B.R. (1960). Functional localization within the amygdaloid complex in the cat. Electroencephalogr. Clin. Neurophysiol. *12*, 1–20.

Uwano, T., Nishijo, H., Ono, T., and Tamura, R. (1995). Neuronal responsiveness to various sensory stimuli, and associative learning in the rat amygdala. Neuroscience *68*, 339–361.

Weinberger, N.M. (1997). Learning-Induced Receptive Field Plasticity in the Primary Auditory Cortex. Semin. Neurosci. *9*, 59–67.

Weinberger, N.M. (2004). SPECIFIC LONG-TERM MEMORY TRACES IN PRIMARY AUDITORY CORTEX. Nat Rev Neurosci *5*, 279–290.

Weinberger, N.M. (2015). New perspectives on the auditory cortex: learning and memory. Handb. Clin. Neurol. *129*, 117–147.

Weinberger, N.M., and Diamond, D.M. (1987). Physiological plasticity in auditory cortex: Rapid induction by learning. Prog. Neurobiol. *29*, 1–55.

Wilensky, A.E., Schafe, G.E., and LeDoux, J.E. (1999). Functional Inactivation of the Amygdala before But Not after Auditory Fear Conditioning Prevents Memory Formation. J. Neurosci. *19*, RC48–RC48.

Yang, Y., Liu, D., Huang, W., Deng, J., Sun, Y., Zuo, Y., and Poo, M. (2016). Selective synaptic remodeling of amygdalocortical connections associated with fear memory. Nat. Neurosci. *19*, 1348–1355.

CHAPTER 3: Brain state modulates frequency tuning in primary auditory cortex

Abstract

Changes in arousal influence cortical sensory representations, but the effects of arousal on frequency tuning and discrimination in the auditory cortex remain unclear. Here we use two-photon Ca2+ imaging in auditory cortex of awake mice to show that heightened arousal, as indexed by pupil dilation, broadens frequency-tuned activity of layer 2/3 pyramidal cells. Sensory representations are less sparse and the tuning of nearby cells more similar when arousal increases. However, as arousal increases, mean shared trial-by-trial variability is reduced such that cell ensembles are better at frequency discrimination.

Introduction

Information processing in sensory cortex is modulated by changes in behavioral states such as those associated with arousal, attention or task engagement (Harris and Thiele, 2011a; Lee and Dan, 2012; McGinley et al., 2015b; Zagha and McCormick, 2014). Indeed, moment-to-moment changes in arousal have strong effects on spontaneous and stimulus evoked firing activity in primary visual cortex (Ayaz et al., 2013; Bennett et al., 2013; Fu et al., 2014; Mineault et al., 2016; Niell and Stryker, 2010; Polack et al., 2013; Reimer et al., 2014; Vinck et al., 2015) and auditory cortex (McGinley et al., 2015a; Schneider et al., 2014; Zhou et al., 2014). In recordings from head-fixed mice, changes in arousal are typically assessed by measurements of pupil diameter or exploratory behavior such as locomotion, with increases in pupil diameter and bouts of running/walking indicating heightened arousal (McGinley et al., 2015a). Interestingly, the transition from quiet wakefulness to locomotion has different effects in visual and auditory cortex: walking/running increases stimulus-driven firing in V1 (Ayaz et al., 2013; Niell and Stryker, 2010; Polack et al., 2013; Saleem et al., 2013; Vinck et al., 2015) and is associated with a decrease in sensory-evoked firing in A1 (McGinley et al., 2015a; Schneider et al., 2014; Zhou et al., 2014). However, heightened arousal does not require movement and

recent work suggests that motor feedback signals to sensory cortex modulate activity differently than arousal tracked by pupillometry during quiet wakefulness (Schneider et al., 2014; Vinck et al., 2015). Despite the potential for arousal to regulate cortical sensory coding, the manner in which changes in brain state influence tuning properties in the auditory cortex remain incomplete, particularly when considering arousal on a finer continuum than a binary classification of active or inactive behavioral states.

In this study, we use pupillometry and Ca2+ imaging to study how fluctuations in arousal in the absence of locomotion modulate frequency coding in A1 of head-fixed mice. Transitions from low to moderate and high arousal levels enhance the strength and reliability of responses to pure tones and increase the tuning broadness of L2/3 pyramidal cells. Although sensory representations become less sparse and signal correlations increase, heightened arousal reduces noise correlations and improves tone discrimination by cell populations.

Results

We used transgenic mice (*Emx-Cre/CamKII-tTA/Ai94(TITL-GCaMP6s*)) and two-photon imaging to study responses to tones in A1 L2/3 pyramidal cells. Prior to recording, head-fixed mice were habituated to sitting quietly for prolonged time periods (1-2 hours) on a static platform. During imaging of A1 in the right hemisphere, mice sat on a passive treadmill that measured movement while a camera simultaneously monitored pupil dilation of the contralateral eye and blocks of pure tones (17 frequencies, 2 – 40 kHz, 1 s duration, 60 dB) were delivered via free-field speaker to the contralateral ear (Figure 3.1A). Over the course of single imaging sessions, pupil diameter routinely fluctuated between constricted and dilated states (Fig. 3.1B). Measurements were normalized to maximum pupil diameter for each recording. Under our recording conditions, mice were stationary for the vast majority of time and while sporadic locomotion bouts were nearly always associated with maximally dilated pupils, mice spent considerable time with pupils just as dilated while stationary (Figure 3.1B-C). As reported by previous studies (McGinley et al., 2015a; Schneider et al., 2014; Zhou et al., 2014), locomotion during hyperarousal resulted in a suppression of tone-evoked activity (Figure 3.2). For all experiments, we excluded from analysis the small number of tone trials during locomotion, thereby limiting our investigation to how different levels of arousal (indexed by pupil diameter) modulate cortical activity.

We examined the influence of arousal on tone-evoked responses by sorting tone trials by the mean pupil diameter during the tone period. While significant tone-evoked responses were rarely observed in individual cells when pupils were most constricted (1-20% of maximal diameter), the same tones elicited robust responses as pupil diameter increased (Figure 3.1D). This reflects the fact that both the amplitude and reliability of tone-evoked responses were strongly dependent on arousal. At best frequency (BF, defined as the frequency eliciting the strongest response in each cell averaged across all pupil diameters), the response strength and trial-to-trial reliability increased by more than 4-fold (Friedman's ANOVA, $P_{strength}<0.0001$,

$P_{reliability}$<0.0001) when pupils were most dilated (81-100% vs. 1-20% maximal diameter (Figure 3.1E$_1$). These changes in response strength led to a marked increase (Friedman's ANOVA, $P_{\%\ of\ tones}$<0.0001) in the broadness of frequency tuning in individual cells: the number of tones eliciting significant responses peaked at moderate arousal levels (41-60% of maximal pupil diameter, Figure 3.1E$_2$). Similar results were obtained with analysis of lifetime sparseness (Friedman's ANOVA, $P_{(1-Sp)}$<0.0001), a measure that does not require thresholding responses (Figure 1.1E$_2$). We next examined whether arousal modulates the shape of frequency tuning curves by centering cell responses at the low arousal BF, defined as the frequency eliciting the strongest response in each cell when averaged across all trials with 1-35% maximal pupil diameter (Figure 3.1F). Intriguingly, increases in arousal widened frequency tuning curves (n=119 cells; two-way ANOVA, $P_{arousal}$<0.0001, $P_{frequency}$<0.0001, $P_{interaction}$<0.0001) in an asymmetric fashion: responses to frequencies higher than the low arousal BF were more strongly enhanced than responses to frequencies lower than the low arousal BF (Figure 3.1F). Importantly, despite these arousal-dependent changes in the symmetry of tuning curves, the BF of individual cells remained stable ($n_{1-35\%}$=119 cells, $n_{66-100\%}$=186 cells, Kolmogorov-Smirnov test, P=0.9411, Figure 3.1F). Taken together, these results indicate that arousal strongly shapes the strength and reliability of tone evoked responses and broadens frequency tuning in A1 layer 2/3 cells.

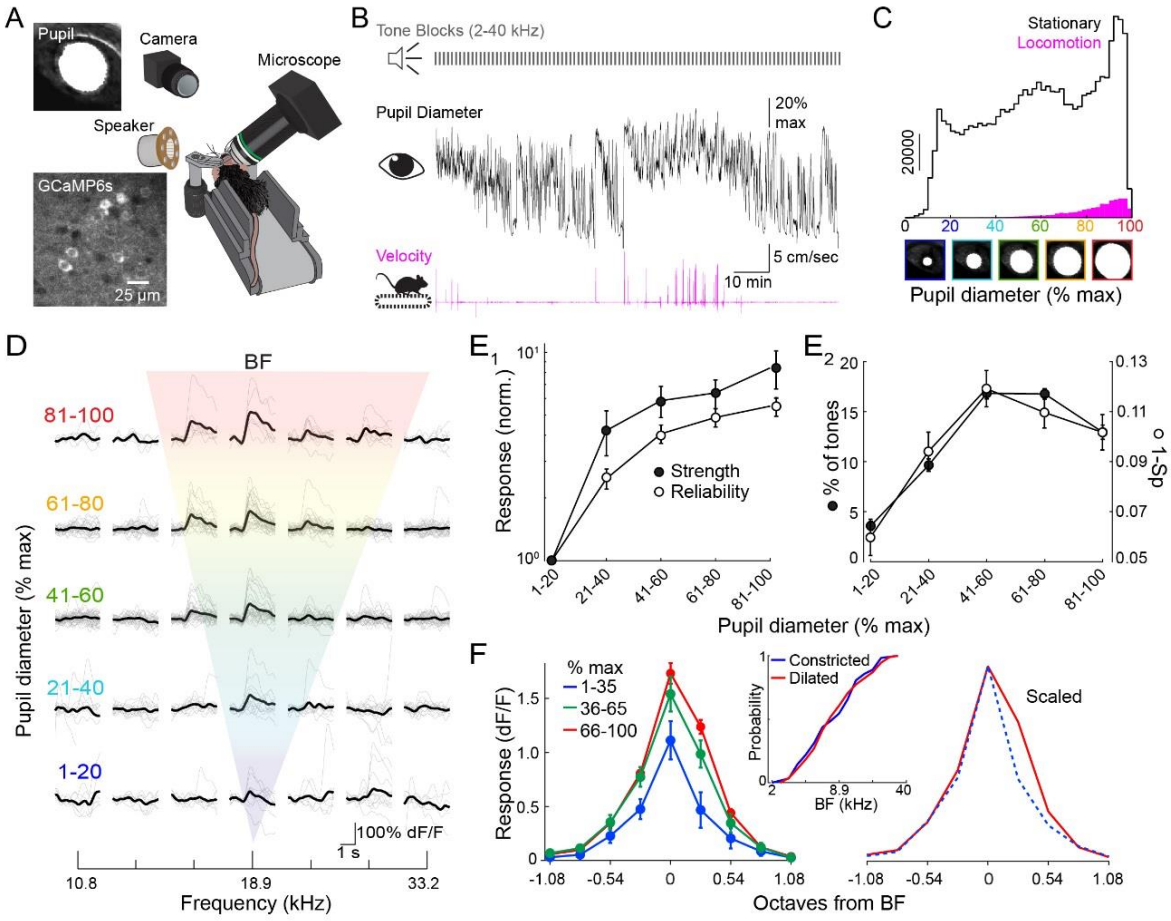

Figure 3.1. Arousal asymmetrically modulates frequency tuning of layer 2/3 pyramidal cells. (A) A high-speed camera and electrostatic speaker were located contralateral to the imaging FOV for pupillometry and tone delivery, respectively. (B) Top, 100 blocks of 17 60 dB pure tones, logarithmically spaced between 2 and 40 kHz, were presented during each imaging session. Middle, pupil diameter constantly fluctuates over a large range. Bottom, locomotion was tracked by a low-friction treadmill. (C) Locomotion only occurs during states of maximal pupil dilation, and mice primarily remained stationary during imaging due to extensive habituation with the setup. (D) Tone responses for a representative cell are modulated by arousal at preferred frequencies. (E1) Best frequency (BF) response strength and reliability monotonically increase with arousal (n=195 cells). BF was defined here as the frequency that evoked the strongest mean responses (integral dF/F) irrespective of arousal state. Response reliability for each cell during each arousal state was quantified as the mean pairwise, trial-by-trial Pearson's correlation coefficient. Response strength and reliability were normalized to each cell's corresponding low arousal (1-20% pupil max) mean value. (E2) Tuning broadness increases with arousal and was measured by either % of tones that evoked statistically significant responses or lifetime sparseness (Sp) subtracted from 1. (F) Left, tuning broadness is modulated asymmetrically by arousal (n=119 cells). BF was defined here as the frequency that evoked the strongest response (integral dF/F) during low arousal (1-35% pupil max). Cells that did not exhibit significant responses during low arousal were excluded. Middle inset, Best frequencies do not shift significantly between low (constricted, 1-35% pupil max) and high

(dilated, 66-100% pupil max) arousal (n_{low}=119 cells, n_{high}=186 cells). Right, tuning curve for low arousal scaled to that of high arousal.

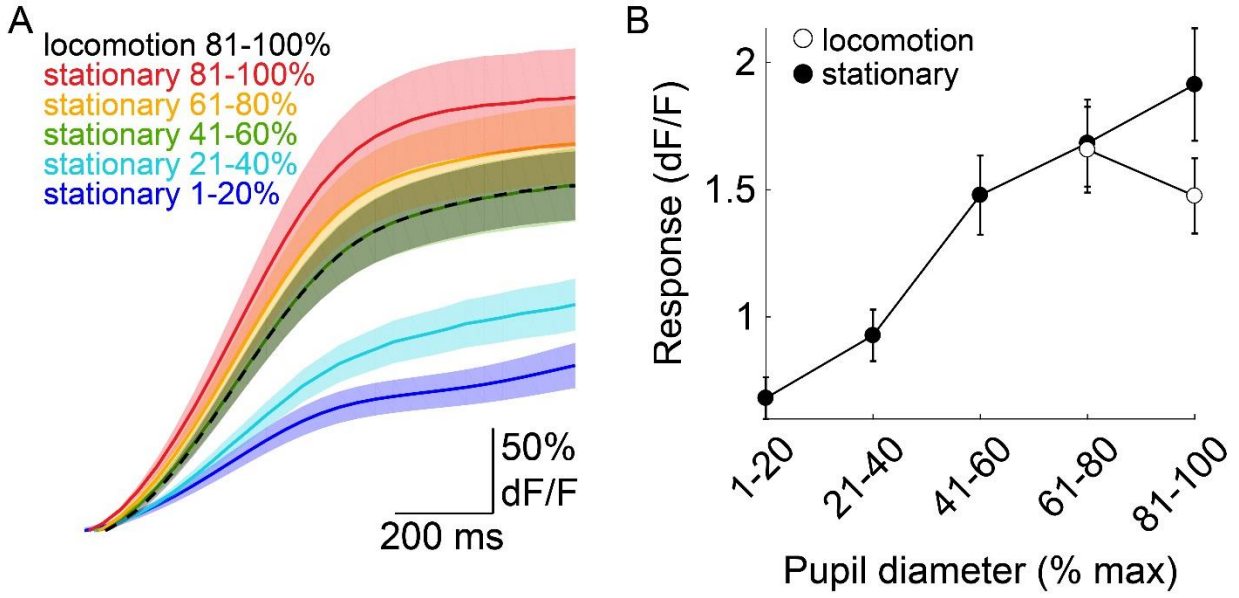

Figure 3.2. Locomotion suppresses tone-evoked activity during hyperarousal. (A) Each cell's response waveforms at BF were averaged together for each brain state (n=140 cells). Cells from experiments in which locomotion did not occur during tone presentations were excluded from this analysis. (B) Response strength (integral dF/F) at BF increases monotonically with arousal in the absence of locomotion, and locomotion during hyperarousal (81-100% pupil max) results in suppression of BF responses (n=140 cells; Student's t-test; P=0.0058).

We next considered how arousal-dependent changes in pyramidal cell response properties contribute to sensory representations in A1. Consistent with the increases in response strength and tuning broadness, the fraction of cells in imaging fields (n = 8 fields, 5 mice) responding to any of the presented tones was strongly dependent on the level of arousal (Friedman's ANOVA, P<0.0001), Figure 3.3A-B). On average, the fraction of tone responsive cells increased from 3.05±0.65% during periods of lowest arousal (1-20% maximal pupil diameter) to 9.17±0.91% during moderate arousal (41-60% maximal diameter), and there was a slight reduction of responses during the periods of highest arousal (81-100% max diameter). These results indicate that arousal shapes the relative sparseness of sensory representations at the population level.

How do the arousal-related changes in sensory representations we observe impact the ability of the L2/3 pyramidal cell population to discriminate tone frequencies? At face value, the reduction in sparseness of activated cells and broadening of frequency tuning should increase overlap in cell ensembles activated by individual tone frequencies. This implies that increases in arousal would degrade rather than improve the ability of A1 L2/3 to discriminate different tone frequencies. To address this issue, we analyzed inter-neuronal correlations that contribute to population coding: signal correlations (r_{signal}), a measure of tuning similarity between pairs of neurons and noise correlations (r_{noise}), a measure of how much the trial-to-trial response variability of a pair of neurons is correlated (Averbeck et al., 2006; Cohen and Kohn, 2011). Consistent with previous studies in auditory cortex (Downer et al., 2015; Issa and Wang, 2013; Rothschild et al., 2010; Winkowski and Kanold, 2013), mean r_{signal} and r_{noise} values were small and positive (n = 4938 cell pairs pooled from 8 experiments, Figure 3.3$C_{1\text{-}2}$). Inter-neuronal correlations were also modulated bidirectionally by arousal (two-way ANOVA, $P_{arousal}<0.0001$, $P_{correlations}<0.0001$, $P_{interaction}<0.0001$). Across all tone-responsive cells, mean r_{signal} increased markedly as pupils became more dilated (Figure 3.3D_1). This indicates that the tuning of L2/3 pyramidal cells became more similar as arousal increased, consistent with the notion that elevations in arousal could degrade frequency discrimination. However, for the same cell pairs, mean r_{noise} tended to fall as arousal increased (Figure 3.3D_1). Previous work has established that reducing r_{noise} should enhance sensory discrimination when cell pairs exhibit more similar tuning, but impair discrimination when tuning is more dissimilar (Averbeck et al., 2006; Cohen and Kohn, 2011; Downer et al., 2015; Gu et al., 2011; Jeanne et al., 2013). Thus, we performed a linear fit on the the r_{signal} values of each cell pair and found that while the majority of pairs increased (n=3086 cell pairs) in r_{signal} with arousal, there was a significant subset of pairs that decreased (n=1852 cell pairs) in r_{signal} with arousal. Intriguingly, we found that arousal-dependent changes in r_{noise} were highly selective: r_{noise} decreased specifically in cell pairs that became more similarly tuned (increase in r_{signal}) as arousal increased (two-way ANOVA,

$P_{arousal}<0.0001$, $P_{correlations}<0.0001$, $P_{interaction}<0.0001$, Figure 3.3D$_2$). In contrast, r_{noise} increased specifically in cell pairs in which elevations in arousal led to a reduction in r_{signal} (two-way ANOVA, $P_{arousal}<0.0001$, $P_{correlations}=0.0664$, $P_{interaction}<0.0001$, Figure 3.3D$_3$). Together, these relationships between r_{signal} and r_{noise} suggest that increases in arousal should enhance frequency discrimination by cell populations in L2/3.

To investigate the net effect of arousal-dependent changes in tone-evoked activity on frequency discrimination, we used a nonlinear classifier to assess layer 2/3 pyramidal cell representations of pure tones. The classifier was trained on 75% of tone trials (randomly selected) in a given experiment, with vectors containing the cells' response strengths (integral dF/F) during each trial, paired with the tone frequency presented during each trial. The remaining 25% of tone trials were then used to test the classifier on accurately decoding which tone frequency was presented during each test trial when given only the cell's response vector during that trial. We repeated the training and testing procedure 100 times. To specifically investigate the contribution of arousal-dependent changes in noise correlations on frequency encoding, the temporal order of responses was shuffled such that noise correlations were abolished while the frequency identity for each tone trial remained unchanged. As expected, the decoder performed above chance level (5.9%) independent of arousal state for both the unshuffled and shuffled datasets. More importantly, decoding accuracy improved significantly (Figure 3.3E) with increased arousal only when noise correlations were intact (two-way ANOVA with post-hoc multiple comparisons, $P_{arousal}=0.0008$, $P_{dataset}<0.0001$, $P_{interaction}=0.1272$). Thus, arousal-dependent changes in noise correlations strongly contribute to enhanced frequency discrimination with increased arousal.

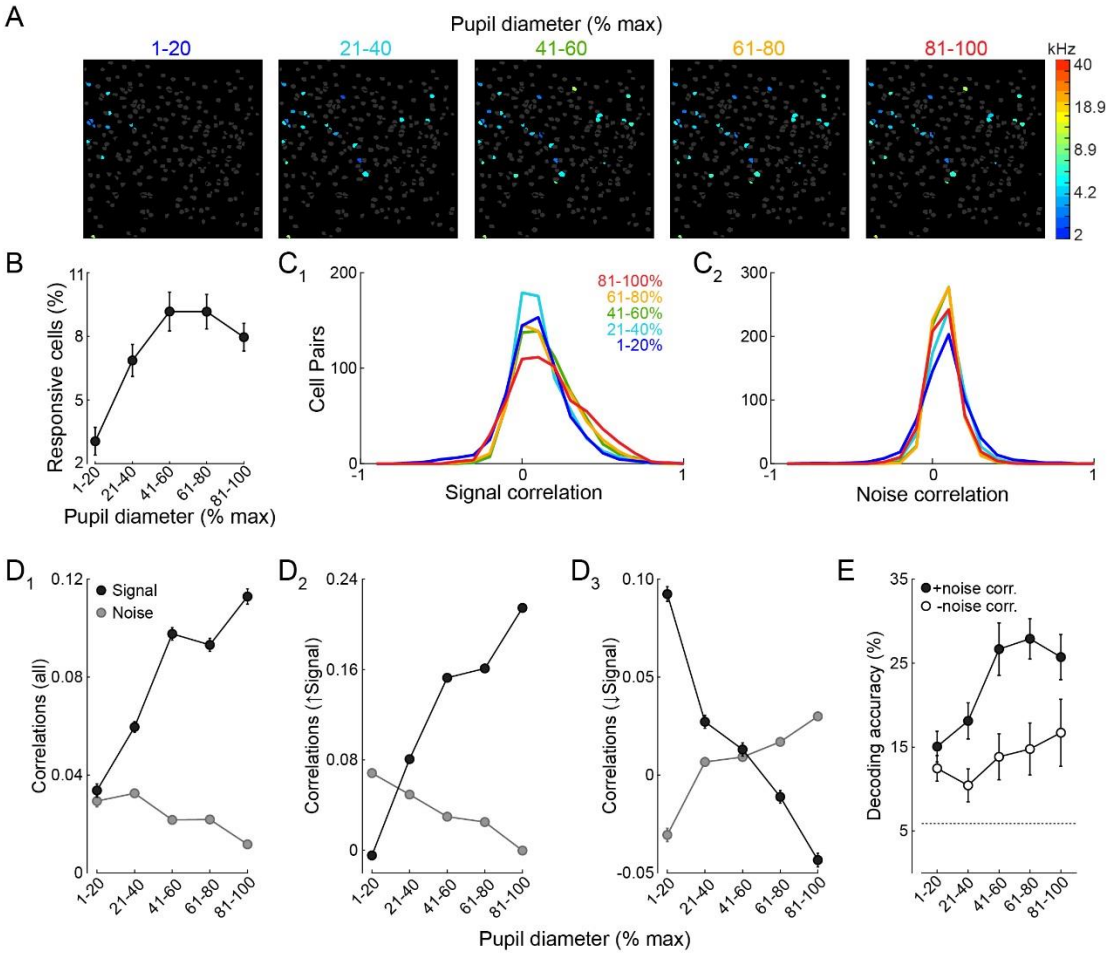

Figure 3.3. Arousal decreases the sparseness of tone representations and modulates inter-neuronal correlations in a manner that ultimately improves frequency discrimination. (A) Increased arousal results in emergence of additional tone-responsive cells (N=8 fields, 5 mice). Each box displays the same representative imaging FOV with tone-responsive neurons color-coded by BF. BF was defined here as the frequency that evoked the strongest mean responses (integral dF/F) irrespective of arousal state. (B) The percentage of cells that are tone-responsive increases with arousal. Increased arousal results in (C1) broader signal correlation distributions and (C2) narrower noise distributions (n=4938 cell pairs). (D1) Mean signal correlations increase and mean noise correlations decrease with arousal (n=4938 cell pairs). (D2) The majority of cell pairs exhibit signal correlations that increase with arousal (n=3086 cell pairs) and noise correlations that decrease with arousal. (D3) Some cell pairs exhibit signal correlations that decrease with arousal (1852 cell pairs), and noise correlations for those pairs increase with arousal. (E) Nonlinear classifier analysis with a K-nearest neighbors algorithm (k=10, standardized Euclidean distance metric, 100 iterations) reveals significant improvement to decoding accuracy as arousal increases. This improvement is only apparent with noise correlations intact. Dotted line represents chance level.

Discussion

We used a combination of pupillometry, locomotion tracking, and two-photon calcium imaging to describe the effects of arousal on frequency tuning and discrimination in awake mouse A1. In the absence of locomotion, increased arousal mediates an enhancement in response strength and reliability of layer 2/3 pyramidal cells that manifests as an asymmetrical increase in tuning broadness. An increase in tuning broadness with arousal was surprising for two reasons. First, previous studies of attention- or arousal-dependent receptive field plasticity in sensory cortices have reported more selective tuning to features. For example, the spectrotemporal response field (STRF) of A1 cells in awake ferrets become more narrowly tuned during attentional engagement in a task compared to during passive behavior (Atiani et al., 2009; Fritz et al., 2003). In the visual cortex, cortical desynchronization—a hallmark of increased arousal—results in smaller spatial receptive fields in V1 of anesthetized cats (Wörgötter et al., 1998). Finally, in a more recent study of V1 evoked activity, orientation tuning becomes more selective with pupil dilation (Reimer et al., 2014).

The second reason an arousal-dependent increase in tuning broadness was unexpected is due to reports of optimal performance on discrimination tasks at intermediate to high arousal states (Yerkes and Dodson, 1908). From a theoretical perspective, increased tuning broadness results in an increase in the overlap of tone representations, which would be predicted to have a detrimental effect on frequency discrimination. However, we also observed changes in population activity that are predicted to improve frequency discrimination (Averbeck et al., 2006; Cohen and Kohn, 2011; Downer et al., 2015; Gu et al., 2011; Jeanne et al., 2013). With increasing arousal, noise correlations decrease for cell pairs that increase in signal correlations and noise correlations increase for cell pairs that decrease in signal correlations. Unsurprisingly, nonlinear classifier analysis revealed improved frequency discrimination with arousal. Thus, while increase in tuning broadness with arousal could, in isolation, negatively affect frequency

discrimination, a concurrent decrease in mean noise correlations provides a counterbalance that ultimately benefits discrimination.

Positive noise correlations are inevitable in a network of neurons that receive common input. In order for mean noise correlations in the cortex to decrease, it is likely that excitatory and inhibitory inputs to a population become more correlated with arousal, thus resulting in negative noise correlations that counter-balance the positive noise correlations associated with common synaptic inputs (Harris and Thiele, 2011). Although this prediction has thus far only been verified theoretically in cortical networks (Renart et al., 2010), concurrent calcium imaging of layer 4 excitatory inputs and local inhibition in A1 layer 2/3 would be one potential approach to addressing this model experimentally.

Finally, the synaptic mechanisms that underlie arousal-dependent modulation of frequency tuning in A1 remain to be determined. The asymmetric increase in tuning broadness observed in this study is not only intriguing but also provides a potential hint for the underlying mechanism. A recent study utilizing whole cell recording in awake mouse A1 has reported a unique process that is more prominent at high frequencies and contributes to lateral inhibition via SOM-mediated “network suppression” of recurrent activity (Kato et al., 2017). We hypothesize that arousal regulates the strength of tone-evoked activity by strongly gating this indirect network inhibition and are currently undertaking *in vivo* whole cell current clamp and voltage clamp recordings to address this possibility.

Experimental Procedures

Animals. Mice between 8 and 16 weeks of age of both genders were used for all experiments. Mice were acquired from Jackson Laboratories (*Emx1-Cre (Jax: 05638), Ai94(TITL-GCaMPs)-D;CaMK2a-tTA (Jax: 024115*)) and housed in a room with a 12:12 reversed light cycle. Experiments were performed during the dark period. Mice had no prior history of experimental procedures that could affect the results. All procedures were in accordance with protocols approved by the UCSD Institutional Animal Care and Use Committee and guidelines of the National Institute of Health.

Chronic window implantation. Mice were anesthetized with isoflurane and injected with dexamethasone (2 mg/kg) intraperitoneally. A custom stainless steel headbar was glued to the skull. Muscle overlying the right auditory cortex was removed and a craniotomy (~2 X 3 mm) was made, leaving the dura intact. A glass window was placed over the craniotomy and secured with Vetbond and dental acrylic. Baytril (10 mg/kg) and buprenorphine (0.1 mg/kg) were injected subcutaneously before mice were returned to their home cages for recovery.

Mouse handling and habituation. Mice were handled for 5 minutes daily for the first 3 days following window implantation. Then, mice were habituation to head fixation on a treadmill under a two-photon microscope for 2 hours a day for 5-7 days.

Sound stimulus presentation. Auditory stimuli were delivered via a free-field electrostatic speaker (ES1: Tucker-Davis Technologies). For intrinsic and calcium imaging, speakers were calibrated over a range of 2-40 kHz to give a flat responses (± 1 dB). For in vivo whole-cell recording, speakers were calibrated over a range of 4-60 kHz. Stimuli were delivered to the ear contralateral to imaging or recording. Auditory stimulus delivery was controlled by software (BControl; http://brodylab.org) running on MATLAB (MathWorks) communicating with a real-time system (RTLinux).

Intrinsic signal imaging. Intrinsic signal imaging was performed through chronic windows 1-3 days before calcium imaging to locate A1. Images were acquired using a tandem

lens macroscope and 12 bit, CCD camera (CCD-1300QF, VDS Vosskühler). Mice were anesthetized with isoflurane. Images of surface vasculature through the chronically implanted window were acquired using green LED illumination (530 nm) and intrinsic signals were recorded (27 Hz) using red illumination (615 nm). Each trial consisted of a 1s baseline followed by a 1 s sound stimulus (70 dB pure tone with a frequency of 3, 10, or 30 kHz, 10-20 trials per frequency) and a 30 s inter-trial interval. Images of reflectance were acquired at 1024 X 1024 pixels (covering ~2.1 x 2.1 mm) and downsampled to 512 x 512 pixels by interpolation. Images during the response period (0.5-2 s from the sound onset) were averaged and divided by the average image during the baseline. Images were averaged across trials and Gaussian filtered.

***In vivo* two-photon calcium imaging.** Calcium imaging was performed within 2-3 weeks following chronic window implantation. Two-photon imaging fields were aligned with the intrinsic signal imaging fields by comparing blood vessel patterns. GCaMP6s was excited at 950 nm (Mai Tai, Newport) and images (512 x 512 pixels covering ~500 x 500 µm) were acquired with a commercial microscope (B-scope, Thorlabs) running ScanImage 4 software using a 16x objective (Nikon) at 28.4 Hz. Images were acquired from L2/3 (120-250 µm below surface) at 2X zoom while 60-100 blocks of 17 randomly-ordered pure tones (60 dB, 1 sec duration, 3 sec inter-trial interval, 2-40 kHz) were presented. Lateral motion was corrected using a phase correlation algorithm (https://github.com/cortex-lab/Suite2P).

Imaging analysis. A cell response to a tone was classified as statistically significant if $p<0.005$ (Wilcoxin Rank Sum) for >85% of trial-pooled timepoints over any continuous 0.5 sec window during the 1 sec tone period, compared to a trial-pooled, 1 sec baseline period immediately preceding the tone period. A cell was classified as tone responsive if responses to at least two tones in at least two of five arousal states (20% bins from 0-100% pupil max) were statistically significant. To measure a cell's strength of response to each tone frequency, the dF/F integral of the mean response of each cell during each arousal state was calculated and normalized to that of its mean response at low arousal (i.e. 1-20% pupil max). To measure a

cell's reliability of response to each tone frequency, the mean pairwise, trial-by-trial Pearson's correlation coefficient during each arousal state was calculated and normalized to the reliability value obtained at low arousal. Tuning broadness for each cell was measured by calculating the % of tones that evoked statistically significant responses during each arousal state. Because % of tones is inherently a binary measure of responsiveness to each tone, tuning broadness was also quantified in terms of lifetime sparseness. Lifetime sparseness (Rolls and Tovee, 1995; Willmore and Tolhurst, 2001), or *Sp*, was calculated as $(1-\{[\sum_{j=1,N} rj/N]^2/[\sum_{j=1,N} r^2_j/N]\})/(1-1/N)$, where r_j was the response peak amplitude of the cell to tone *j*, and *N* was the total number of tones. $(1 - Sp)$ provides a measure of how much the response probability of a neuron is distributed equally among all tones (non-selective: $1 - Sp = 1$) versus attributable entirely to one tone (highly selective: $1 - Sp = 0$).

Analysis of population activity. Total correlations, defined as the sum of signal correlations and noise correlations, were quantified by first creating a trial-by-trial tone response vector for each arousal state for each cell. Each value within a response vector was calculated by taking the dF/F integral during the 1 second tone period of each trial. To calculate signal correlations, the temporal order of each cell's responses to repeated presentations of each tone were shuffled within the cell's response vector, abolishing noise correlations while maintaining trial-by-trial stimulus identity. Total and signal correlations were obtained by calculating the Pearson's correlation coefficients for the unshuffled response vectors and shuffled response vectors, respectively, of pairs of cells from the same imaging session. A noise correlation value for each pair of cells from each imaging session was obtained by subtracting their signal correlation value from their total correlation value. To determine if arousal modulates noise correlations in a manner that is dependent on how arousal modulates tuning similarity, the mean noise correlations during each arousal state were calculated separately for pairs of cells with signal correlations that generally increased with arousal (slope > 0 using MATLAB function

polyfit()) and for pairs of cells with signal correlations that generally decreased with arousal (slope < 0).

Decoder analysis. To test whether the effects of arousal improve population coding of tone frequency, a population response matrix for each tone trial was created from the response vectors for all cells within each imaging session. The population response matrices for a subset of randomly selected tone trials (75% of total trials) were used to train a K-nearest neighbors classifier (k = 10 trials; standardized Euclidean distance metric) before testing the performance of the classifier on the remaining 25% of tone trials. The % correctly decoded trials was calculated from 100 iterations of this process.

Pupilometry and locomotion tracking. The eye contralateral to imaging or recording was monitored via a compact, high-speed camera (BFLY-U3-05S2M-CS, Point Grey) with 50 mm fixed focal lens (M5018-MP2, Computar). Locomotion was monitored by a low friction, rodent-drive treadmill fitted with a rotary encoder (Janelia). Pupil measurements and velocity were acquired via the open-source software Bonsai (bonsai-rx.org).

Analysis of pupil and locomotion data. Raw pupil diameter was smoothed using a moving average filter over a window of 1 sec, then normalized to the maximum value during a given imaging session or series of recordings from the same mouse. Locomotion epochs (non-zero velocity for >0.5 s) during calcium imaging were excluded from analysis in order to specifically investigate the effects of arousal on tone-evoked responses.

Quantification and statistics. All data are presented as mean ± SEM. Statistically significant differences between conditions were determined using standard parametric or nonparametric tests in MATLAB. All n values refer to the number of cells except when explicitly stated that the n is referring to the number of mice. Experiments were not performed blind. Sample sizes were not predetermined by statistical methods, but were based on those commonly used in the field.

Data and software availability. The custom MATLAB code will be made available upon reasonable request.

References

Atiani, S., Elhilali, M., David, S. V, Fritz, J.B., and Shamma, S.A. (2009). Task difficulty and performance induce diverse adaptive patterns in gain and shape of primary auditory cortical receptive fields. Neuron *61*, 467–480.

Averbeck, B.B., Latham, P.E., and Pouget, A. (2006). Neural correlations, population coding and computation. Nat. Rev. Neurosci. *7*, 358–366.

Ayaz, A., Saleem, A.B., Schölvinck, M.L., and Carandini, M. (2013). Locomotion Controls Spatial Integration in Mouse Visual Cortex. Curr. Biol. *23*, 890–894.

Bennett, C., Arroyo, S., and Hestrin, S. (2013). Subthreshold Mechanisms Underlying State-Dependent Modulation of Visual Responses. Neuron *80*, 350–357.

Cohen, M.R., and Kohn, A. (2011). Measuring and interpreting neuronal correlations. Nat. Neurosci. *14*, 811–819.

Downer, J.D., Niwa, M., and Sutter, M.L. (2015). Task engagement selectively modulates neural correlations in primary auditory cortex. J. Neurosci. *35*, 7565–7574.

Fritz, J., Shamma, S., Elhilali, M., and Klein, D. (2003). Rapid task-related plasticity of spectrotemporal receptive fields in primary auditory cortex. Nat. Neurosci. *6*, 1216–1223.

Fu, Y., Tucciarone, J.M., Espinosa, J.S., Sheng, N., Darcy, D.P., Nicoll, R.A., Huang, Z.J., and Stryker, M.P. (2014). A cortical circuit for gain control by behavioral state. Cell *156*, 1139–1152.

Gu, Y., Liu, S., Fetsch, C.R., Yang, Y., Fok, S., Sunkara, A., DeAngelis, G.C., and Angelaki, D.E. (2011). Perceptual learning reduces interneuronal correlations in macaque visual cortex. Neuron *71*, 750–761.

Harris, K.D., and Thiele, A. (2011a). Cortical state and attention. Nat. Rev. Neurosci. *12*, 509–523.

Harris, K.D., and Thiele, A. (2011b). Cortical state and attention. Nat. Rev. Neurosci. *12*, 509–523.

Issa, E.B., and Wang, X. (2013). Increased neural correlations in primate auditory cortex during slow-wave sleep. J. Neurophysiol. *109*, 2732–2738.

Jeanne, J.M., Sharpee, T.O., and Gentner, T.Q. (2013). Associative Learning Enhances Population Coding by Inverting Interneuronal Correlation Patterns. Neuron *78*, 352–363.

Kato, H.K., Asinof, S.K., and Isaacson, J.S. (2017). Network-Level Control of Frequency Tuning in Auditory Cortex. Neuron *95*.

Lee, S.-H., and Dan, Y. (2012). Neuromodulation of brain states. Neuron *76*, 209–222.

McGinley, M.J., David, S. V., and McCormick, D.A. (2015a). Cortical Membrane Potential Signature of Optimal States for Sensory Signal Detection. Neuron *87*, 179–192.

McGinley, M.J., Vinck, M., Reimer, J., Batista-Brito, R., Zagha, E., Cadwell, C.R., Tolias, A.S., Cardin, J.A., and McCormick, D.A. (2015b). Waking State: Rapid Variations Modulate Neural and Behavioral Responses. Neuron *87*, 1143–1161.

Mineault, P.J., Tring, E., Trachtenberg, J.T., and Ringach, D.L. (2016). Enhanced Spatial Resolution During Locomotion and Heightened Attention in Mouse Primary Visual Cortex. J. Neurosci. *36*, 6382–6392.

Niell, C.M., and Stryker, M.P. (2010). Modulation of Visual Responses by Behavioral State in Mouse Visual Cortex. Neuron *65*, 472–479.

Polack, P.-O., Friedman, J., and Golshani, P. (2013). Cellular mechanisms of brain-state-dependent gain modulation in visual cortex. Nat. Neurosci. *16*, 1331–1339.

Reimer, J., Froudarakis, E., Cadwell, C.R., Yatsenko, D., Denfield, G.H., and Tolias, A.S. (2014). Pupil fluctuations track fast switching of cortical states during quiet wakefulness. Neuron *84*, 355–362.

Renart, A., de la Rocha, J., Bartho, P., Hollender, L., Parga, N., Reyes, A., and Harris, K.D. (2010). The asynchronous state in cortical circuits. Science *327*, 587–590.

Rolls, E.T., and Tovee, M.J. (1995). Sparseness of the neuronal representation of stimuli in the primate temporal visual cortex. J. Neurophysiol. *73*, 713–726.

Rothschild, G., Nelken, I., and Mizrahi, A. (2010). Functional organization and population dynamics in the mouse primary auditory cortex. Nat. Neurosci. *13*, 353–360.

Saleem, A.B., Ayaz, A., Jeffery, K.J., Harris, K.D., and Carandini, M. (2013). Integration of visual motion and locomotion in mouse visual cortex. Nat. Neurosci. *16*, 1864–1869.

Schneider, D.M., Nelson, A., and Mooney, R. (2014). A synaptic and circuit basis for corollary discharge in the auditory cortex.

Vinck, M., Batista-Brito, R., Knoblich, U., and Cardin, J.A. (2015). Arousal and locomotion make distinct contributions to cortical activity patterns and visual encoding. Neuron *86*, 740–754.

Willmore, B., and Tolhurst, D.J. (2001). Characterizing the sparseness of neural codes. Network *12*, 255–270.

Winkowski, D.E., and Kanold, P.O. (2013). Laminar transformation of frequency organization in auditory cortex. J. Neurosci. *33*, 1498–1508.

Wörgötter, F., Suder, K., Zhao, Y., Kerscher, N., Eysel, U.T., and Funke, K. (1998). State-dependent receptive-field restructuring in the visual cortex. Nat. 1998 3966707 *396*, 165.

Yerkes, R.M., and Dodson, J.D. (1908). The relation of strength of stimulus to rapidity of habit-formation. J. Comp. Neurol. Psychol. *18*, 459–482.

Zagha, E., and McCormick, D.A. (2014). Neural control of brain state. Curr. Opin. Neurobiol. *29*, 178–186.

Zhou, M., Liang, F., Xiong, X.R., Li, L., Li, H., Xiao, Z., Tao, H.W., and Zhang, L.I. (2014).

Scaling down of balanced excitation and inhibition by active behavioral states in auditory cortex. Nat. Neurosci. *17*, 841–850.

CHAPTER 4: Pei2P MATLAB analysis pipeline for longitudinal, dual channel Ca^{2+} imaging

Overview

Pei2P is a MATLAB analysis pipeline for longitudinal, dual channel calcium imaging experiments. Awake mice are head-fixed under a two-photon microscope and imaged over several sessions per day for several days. The Pei2P pipeline begins with image registration to correct for movement during imaging followed by semi-automated detection of regions of interest (ROIs), synchronization of behavior and imaging data, and detection of sound stimulus-evoked excitation and suppression. The image registration portion of the code is adapted from Marius Pachitariu's Suite2P 2016 release (UCL). Subsequent analysis scripts were written by Pei-Ann Lin, expanding upon MATLAB code written by Hiroyuki Kato (UNC) while completing his post-doc in the Isaacson lab. Scripts and documentation are not guaranteed to be free of mistakes—use at your own risk!

Original Suite2P documentation: https://github.com/cortex-lab/Suite2P.

Image Registration algorithmic details: https://www.biorxiv.org/content/10.1101/061507v2.full

Installation

1. Install MATLAB 2017a.

2. Copy the entire Pei2P folder to your local MATLAB directory.

3. Browse for the Pei2P folder in your directory by going to Set Path > Add with Subfolders…

Note on MATLAB Versions

All scripts in this package are verified as compatible with MATLAB 2017a but have not been fully tested on any older or newer versions.

Experiment database files

For each step of the analysis pipeline, the “master” file calls a database (Table 4.1) by its filename. Save your database files in the “Step1_Databases folder of the Pei2P directory.

Recommended Filename	Description	Database Example

MouseID_IndividualSessions
e.g.
PL0404_IndividualSessions
	Each entry in this database will be a single imaging session. This database will be used for initial RIGID registration of images.	i = 0;
		
		i = i+1;
		db(i).date = '190417';
		db(i).mouse_name = 'PL0404';
		db(i).region = 'region1_L2';
		db(i).sessions = {'auditoryscreen1'};
		
		i = i+1;
		db(i).date = '190417';
		db(i).mouse_name = 'PL0404';
		db(i).region = 'region1_L2';
		db(i).sessions = {'habituation1'};
		
		i = i+1;
		db(i).date = '190417';
		db(i).mouse_name = 'PL0404';
		db(i).region = 'region1_L2';
		db(i).sessions = {'conditioning1'};
		
		for i = 1:length(db)
		db(i).gchannel = 1; % GCaMP is always Ch1
		end

MouseID_AllSessions
e.g. PL0404_AllSessions
	Each entry in this database will include all imaging sessions that need to be analyzed as one longitudinal experiment. This database will be used for NON-RIGID registration of images.	i = 0;
		
		i = i+1;
		db(i).date = {'190417','190418','190419','190420','190421'};
		db(i).mouse_name = 'PL0404';
		db(i).region = 'region1_L2';
		db(i).sessions = {{'auditoryscreen1','habituation1','conditioning1'},...
		{'auditoryscreen2','retrieval1','conditioning2'},...
		{'auditoryscreen3','retrieval2','conditioning3'}};
		
		for i = 1:length(db)
		db(i).gchannel = 1; % GCaMP is always Ch1
		end

DatasetID_ProjectID
e.g. LA-A2_AmygdalaProject
	Each entry in this database will be the AllSessions entry for a longitudinal experiment. This database will be used for analysis after both initial rigid registration and subsequent non-rigid registration have been completed.	i = 0;
		
		i = i+1;
		db(i).date = {'190417','190418','190419','190420','190421'};
		db(i).mouse_name = 'PL0404';
		db(i).region = 'region1_L2';
		db(i).sessions = {{'auditoryscreen1','habituation1','conditioning1'},...
		{'auditoryscreen2','retrieval1','conditioning2'},...
		{'auditoryscreen3','retrieval2','conditioning3'}};
		
		i = i+1;
		db(i).date = {'190402','190403','190404','190405'};
		db(i).mouse_name = 'CS0321';
		db(i).region = 'region1_L2';
		db(i).sessions = {{'auditoryscreen1','habituation1','conditioning1'},...
		{'auditoryscreen2','retrieval1','conditioning2'},...
		{'auditoryscreen3','retrieval2','conditioning3'}};
		
		for i = 1:length(db)
		db(i).gchannel = 1; % GCaMP is always Ch1
		end

Table 4.1. Example Pei2P experiment database files.

Rigid image registration

MotionCorrection_master

When imaging awake mice, there is often translation in the x-y plane due to movement. Suite2P uses a phase correlation algorithm to correct for movement and align images across time. For dual channel experiments, raw tiffs will be split into separate .tif files for each channel prior to image registration. The copied (one-channel) or split (two-channel) raw tiffs are deleted after image registration is completed. Only one channel is used for image registration (default is channel 1), and the obtained image registration values are applied to correct for movement in both channels for two-channel experiments.

Inputs

- Directories, filepaths, and database filename should all be adjusted according to your system
- Raw imaging data should be saved in tif format with the following folder structure: …\date\mouse_name\regionX_layerY\sessionname*.tif

Outputs

- regop file (contains image registration values for motion correction)
- correctedTiffs (folder of motion corrected tiffs for each functional imaging channel)
- summovie100.tif (image stacks where each frame is 100 motion corrected raw frames summed together; ~3 seconds of data per frame when imaging at 30 fps)
- maxproj.tif (max projection of summovie100.tif

Runtime

Performance clocked on IsaacsonPC7 for a dual channel, 500 frames/channel tif:

- splitChannels: 21 seconds
- MotionCorrection_pipeline: 20 seconds
- createCorrected: 25 seconds

Non-rigid image registration

MotionCorrection2_master

When imaging awake mice across multiple sessions and days, there is often translation in the x-y plane that requires non-rigid motion correction (due to rotational and angular differences in head fixation position). Suite2P uses a phase correlation algorithm to correct for movement and align images across time after first splitting the FOV into equally sized subsections (default is a 5 by 5 grid). The maxproj.tif images obtained from running MotionCorrection_master are used for calculating image registration values across sessions in a longitudinal imaging experiment. For two-channel experiments, only one channel is used for image registration (default is channel 1), and the obtained image registration values are applied to correct for movement in both channels.

Inputs

- Directories, filepaths, and database filename should all be adjusted according to your system
- CorrectedTiffs output by MotionCorrect_master

Outputs

- regop file (contains image registration values for motion correction)
- correctedTiffs (folder of motion corrected tiffs for each functional imaging channel)
- summovie100.tif for each experiment day and overall
- maxproj.tif (max projection of the summovie100.tif)

Runtime

Performance clocked on IsaacsonPC7 for a dual channel, 500 frames/channel tif:

- motionCorrect2_pipeline: 19 seconds
- motionCorrect2_create_corrected: 25 seconds

Region of interest (ROI) detection

ROI_Detection_master

The most important parameter to set when performing ROI detection is the estimated diameter (parameters.diameter) of the ROIs you are seeking to detect. The optimal diameter can vary between different calcium indicators, ScanImage zoom factors, and cell compartments. Additional information about optimizing ROI detection parameters can be found in the original Suite2P documentation on Github.

Inputs

- Directories, filepaths, and database filename should all be adjusted according to your system
- Binary file output by MotionCorrect2_master
-

Outputs

- F_*.mat file containing stat, a structure including iscell label, ROI pixel indices, ROI signals, neuropil signals, etc.

ROI inspection, clustering, and refinement

Suite2P ROI inspection (new_main_2ch)

This GUI loads a F*.mat file and allows the user to visualize and reject ROIs detected by Suite2P. Instructions for using the GUI can be accessed by pressing the “DON’T PANIC” button upon loading the GUI. By clicking “Load plane”, user is prompted to select a F*.mat file and then a maxproj.tif file. Note that the code has been altered to show the max projection image for the experiment when keyboard shortcut (t) is activated. The processed ROIs are output as a F*_proc.mat file.

ROI clustering by cross-correlation (autoClusterGUI)

This GUI is adapted from Bill Connelly’s join_axon GUI (http://www.billconnelly.net/?p=471). Clustering ROIs is optional and typically only desirable when analyzing axons and dendrites. This GUI loads a F*_proc.mat file and allows the user to visualize and cluster ROIs using a threshold cross correlation value (R threshold). The recommended cutoff is 0.6 for axon bouton clustering. Filter width can be increased for more aggressive smoothing of data. Recommended filtering window is 1 to 1.5 s (30-45 frames at 30 fps). The processed clusters are output as a F*_proc_clust.mat file.

Conversion of ROI masks to polygons (processROIs_master)

Suite2P and autoClusterGUI save ROIs as masks. In order to manually refine ROIs, the masks must be converted to polygons. Output is saved as cellbody_Suite2P_axons.roi or cellbody_Suite2P_somas.roi in the same directory as the F*_proc_clust.mat and F*_proc.mat files.

Final inspection of manual refinement of ROIs and Clusters (ROIandClusterInspect)

This GUI allows for adding new ROIs, deleting ROIs, editing existing ROIs, and clustering ROIs. First, a maxproj.tif or summovie100.tif file is loaded by clicking “Browse”. Then, a cellbody_Suite2P_*.roi file is loaded to visualize ROI polygons. Individual ROIs can be selected from the GUI ROI list or by clicking on the ROI of interest in the image figure. Multiple ROIs can be selected using the Ctrl keyboard shortcut and clicking ROIs of interest in the GUI ROI list. Multiple selected clusters or ROIs can be clustered together by clicking the “Combine Clusters” button.

After ROIs or clusters are manually refined, neuropil (“background”) ROIs must be created and saved by clicking the “Draw Background ROIs” button. Background ROI pixels are selected from an annulus formed around each ROI, excluding any pixels that are part of other ROIs. Once the background ROIs appear (magenta outlines), click the “Fix BG ROIs” button. A background ROIs will turn green or yellow if enough non-ROI background pixels are detected around a given ROI. ROIs that are not surrounded by enough background pixels will turn red. The command window will list the ROIs that fall in this category. The user can then choose to select each of those ROIs, click the “Replace BG ROI” button, and draw a new polygon on the image figure to replace the insufficient background ROI. Increasing the outer radius of the background ROIs and re-drawing will typically result in fewer background ROIs rejected due to insufficient pixels. ROIs and background ROIs are saved as cellbody_channelX.roi.

ROI Labels

Once ROIs and background ROIs have been finalized and successfully saved, clicking the “Open ROI Label Maker” button will open a new GUI. In the label maker GUI, the user can again select ROIs or clusters one or more at a time, then select a label (e.g. PV+ cell) and click the “Apply Label” button. Labels are saved as labels_channelX.roilabel.

Signal detection

Obtaining ROI fluorescence signals (Signal_Detection_master)

Before extracting the fluorescence signal for each ROI and background ROI, overlapping regions are found and excluded by the function refineROIs. The fluorescence value at each timepoint is measured as the average pixel intensity across a given ROI mask. Note that even with parallel processing activated, the runtime of Signal_Detection_master can be significant depending on the number of available physical processor cores, number of ROIs or clusters, and the number of imaging frames.

Pre-analysis

ScanImage Metadata (saveStackInfo)

The function saveStackInfo extracts and stores the ScanImage framerate and number of channels for each imaging session.

Ephus Sync Signals (createXSG)

Ephus is the software used during data acquisition to sync imaging with stimulus presentation by recording the Dispatcher bitcode signal (trial initiation and sound starts) and ScanImage frame triggers simultaneously. For each imaging session, the function createXSG extracts the bitcode and frame trigger data stored in separate xsglog files and saves together as one data structure.

Dispatcher Sound Trial Information (getTrialInfo)

Dispatcher is the software used to deliver stimuli during imaging experiments along with a bitcode signal to Ephus. The function getTrialInfo reads the sound information from the Dispatcher file and converts sounding timing into behavior frame numbers.

Bonsai Behavior Data (getBehaviorData)

Bonsai is an open-source software (https://bonsai-rx.org/) used to acquire a variety of signals such as bitcode delivered from Dispatcher, images of the mouse's pupil from a high-speed USB camera, and mouse running velocity from an Arduino-interfaced rotary encoder. The function getBehaviorData reads the Dispatcher bitcode acquired by Bonsai and Ephus in order to synchronize behavior data with imaging and sound stimulus delivery. Outputs currently include pupil diameter and running velocity measured with a variety of metrics during each sound trial, the stimulus frequency set, and the stimulus sound pressure level set. If

parameters.plotFigs is set to true, getBehaviorData will also output figures for pupil dilation and changes in running speed in response to sound stimuli.

ScanImage Frametags (getFrameTags)

Occasionally, ScanImage drops frames during acquisition. The function getFrameTags iterates through the image files to make sure that the actual number of frames matches the total number of frames expected by reading frametags from the ScanImage metadata. Indexes for dropped frames are stored and saved to be excluded when concatenating raw traces across all image files for a given imaging session.

Movement Detection (detectMovement)

Due to sharp fast movements by the mouse during imaging (i.e. during delivery of tailshock), some frames may be aligned incorrectly after image registration. The function detectMovement determines “jumpframes” by noting x-y offsets detected during image registration that are of high velocity (occurring over a low number of frame). Indexes for “jumpframes” are stored and saved to be excluded when concatenating raw traces across all image files for a given imaging session.

Raw Traces (concatenateResults)

The raw traces for each ROI are concatenated together across all image files for a given imaging session by the function concatenateResults. Values at dropped frames and “jumpframes” are set to NaN.

Processed Traces (processTraces)

To obtain final dF/F signals for each ROI, the function processTraces first subtracts out the majority of background neuropil signal (typically 90%) from the ROI signals. Then, a slow,

drifting baseline for each ROI signal is estimated by iterating through a process of excluding likely “active” periods of a trace and smoothing by filtering. Each raw ROI signal is then normalized to its respective estimated drifting baseline to obtain dF/F.

Cells that are very dim are then detected and rejected if the ratio of the estimated drifting baseline for an ROI to the estimated drifting baseline for its background ROI is not sufficiently large (default cutoff is 103%). Rejection labels are saved into new ROI label files.

Activity detection

ActivityDetection_master

In order to determine which ROIs are sound responsive, a Wilcoxin rank sum test is used to categorize whether an evoked response to a particular tone frequency includes significant excitation and/or suppression. The same procedure can also be used to determine whether an evoked response to a particular tone frequency is significantly different from that of another tone frequency.

The Wilcoxin rank sum test assesses whether a baseline population of dF/F values is significantly different from a sufficient portion of the corresponding response population of dF/F values. In brief, the procedure is as follows:

1. During a baseline period with equal duration to and immediately preceding a tone presentation period, all dF/F values are pooled across time and across trials.

2. For each timepoint during the tone presentation period, the dF/F values across trials are pooled. If the p-value exceeds alphaVal (recommended value is 0.005 to account for multiple comparisons) for a sufficient amount of non-consecutive time points (default is 85%) within a given response window (default is 0.5 s window), Criteria 1 is deemed as true for that response.

3. For detecting excitation, if the trial-averaged dF/F trace during any window that met Criteria 1 exceeds the trial-averaged and time-averaged baseline value by more than a certain user-determined threshold (default is a dF/F value of 1), Excitation Criteria 2 is deemed as true for this response. If Criteria 1 and Excitation Criteria 2 are both true for a given a response, the ROI is deemed as excited by the presented tone.

4. For detecting suppression, if the trial-averaged dF/F trace during any window that met Criteria 1 is less than the trial-averaged and time-averaged baseline value by more than a certain user-determined threshold (default is a dF/F value of -1), Suppression Criteria 2 is deemed as true for this response. If Criteria 1 and Suppression Criteria 2 are both true for a given a response, the ROI is deemed as suppressed by the presented tone.

5. If an ROI is significantly responsive to a certain amount of the set of presented tones (default is 30%), the ROI is deemed as sound responsive.

Tips for users

- If planning on imaging the same FOV over more than one day, run rigid image registration (MotionCorrection_master) immediately after acquiring data for the first day's imaging sessions. You will then be able to use the maxproj.tif files to help locate the same FOV (particularly the z-plane) on subsequent days of imaging.
- For optimizing ROI detection, the expected diameter of ROIs is the most important parameter to set. This value varies with the ScanImage zoom factor and of course differs between detecting dendrites, boutons, and somas.
- ROI detection does not perform well when combining non-continuous imaging experiments. The user should consider performing ROI detection over all imaging sessions *excluding non-continuous imaging sessions* and manually refining and adding ROIs that are present in the excluded sessions.
- To save disk space, delete the correctedTiffs folders created for individual imaging sessions by MotionCorrect_master once MotionCorrect2_master output has been used to successfully register images across sessions.

Future Directions

ROI Clustering

For clustering axon boutons or dendritic branches, the Pei2P pipeline currently contains two options: clustering using a simple cross-correlation threshold value (autoClusterGUI) and manually clustering based on visualizing maxproj.tif or summovie100.tif (ClusterInspect). The large amount of time and effort to cluster using ClusterInspect is nearly prohibitive, so future users may want to explore additional quantitative methods for clustering or improving the speed of ClusterInspect.

Signal Detection

Currently, the runtime for Signal_Detection_master is significantly longer than that of Suite2P. Signal_Detection_master is used simply due to limited flexibility in refining ROIs in the Suite2P new_main_2ch GUI. Future users may want to add additional functionality to the Suite2P scripts in order to utilize faster extraction of fluorescence signal in Suite2P.